MEASUREMENT OF MEMBRANE RIGIDITY AND ITS MODULATION BY THE VESICLE TRAFFICKING PROTEIN SAR1

by

ANDREW FRANCIS LOFTUS

A DISSERTATION

Presented to the Department of Chemistry and Biochemistry
and the Graduate School of the University of Oregon
in partial fulfillment of the requirements
for the degree of
Doctor of Philosophy

March 2014

DISSERTATION APPROVAL PAGE

Student: Andrew Francis Loftus

Title: Measurement of Membrane Rigidity and Its Modulation by the Vesicle Trafficking Protein Sar1

This dissertation has been accepted and approved in partial fulfillment of the requirements for the Doctor of Philosophy degree in the Department of Chemistry and Biochemistry by:

Victoria DeRose	Chairperson
Raghuveer Parthasarathy	Advisor
Bradley Nolen	Core Member
Tom Stevens	Core Member
Eric Corwin	Institutional Representative

and

Kimberly Andrews Espy	Vice President for Research and Innovation; Dean of the Graduate School

Original approval signatures are on file with the University of Oregon Graduate School.

Degree awarded March 2014

© 2014 Andrew Francis Loftus

DISSERTATION ABSTRACT

Andrew Francis Loftus

Doctor of Philosophy

Department of Chemistry and Biochemistry

March 2014

Title: Measurement of Membrane Rigidity and Its Modulation by the Vesicle Trafficking Protein Sar1

Sculpting membranes into dynamic, curved shapes is central to intracellular cargo trafficking and other cellular functions. However, generation of membrane curvature during trafficking involves lipids and membrane-associated proteins; current mechanisms focus on creating rigid cages, curved scaffolds, or membrane surface area changes by proteins. This dissertation provides an alternative mechanistic example for the control of membrane deformations, involving modulation of membrane material properties. Sar1, a GTPase of the COPII family, regulates vesicle trafficking from the endoplasmic reticulum. We find that Sar1p lowers the rigidity of the lipid bilayer membrane to which it binds. We examine the behavior of *Saccharomyces cerevisiae* Sar1 (Sar1p) and *Homo sapiens* paralogs of Sar1 (Sar1A and Sar1B). Like Sar1p, human Sar1s lower membrane rigidity. Unlike Sar1p, the rigidity is not a monotonically decreasing function of concentration. At high concentrations, we find increased bending rigidity and decreased protein mobility. These features imply a model in which human Sar1 clustering governs membrane mechanical properties.

Membrane rigidity measurements remain rare, however, and show a large variance, a situation that can be addressed by improving techniques and comparing

disparate techniques applied to the same systems. I introduce applying selective plane illumination microscopy (SPIM) to image thermal fluctuations of giant vesicles. SPIM's optical sectioning enables high-speed fluorescence imaging of freely suspended vesicles and quantification of edge localization precision, yielding robust fluctuation spectra and rigidity estimates. For lipid-only membranes and membranes bound by the intracellular trafficking protein Sar1p, we show rigidity values from giant unilamellar vesicle (GUV) fluctuations in close agreement with those derived from our independent assay based on membrane tether pulling. We also show that a model of homogeneous quasi-spherical vesicles poorly fits fluctuation spectra of vesicles bound by Sar1A at high concentrations, suggesting that SPIM-based analysis can offer insights into spatially inhomogeneous properties.

I conclude by discussing our current work on amphipathic alpha helices, their ability to reduce membrane rigidity, and our hopes to create artificial helical structures capable of mimicking trafficking systems. Supplemental videos represent membrane disintegration with Sar1p and fluctuations of membrane only and Sar1p incubated vesicles.

This dissertation contains previously published co-authored material.

CURRICULUM VITAE

NAME OF AUTHOR: Andrew Loftus

GRADUATE AND UNDERGRADUATE SCHOOLS ATTENDED:

University of Oregon, Eugene, OR
University of Richmond, Richmond, VA

DEGREES AWARDED:

Doctor of Philosophy, Chemistry, 2014 University of Oregon
Bachelor of Science, ACS certified, Chemistry, 2008 University of Richmond

AREAS OF SPECIAL INTEREST:

Biophysics
Biochemistry

PROFESSIONAL EXPERIENCE:

Scientist (Intern), Life Technologies (Molecular Probes), Eugene, OR, Summer 2013

Graduate Teaching Assistant, Department of Chemistry, University of Oregon, Eugene, OR, 2008-2009

GRANTS, AWARDS, AND HONORS:

NSF-IGERT Fellowship, University of Oregon, 2010

Jean Dreyfus Boissevain Undergraduate Scholarship for Excellence in Chemistry, University of Richmond 2007

HHMI Scholar, University of Richmond, 2005 and 2006

PUBLICATIONS:

Loftus, A.F.; Noreng, S.; Hsieh, V.; Parthasarathy, R., Robust measurement of membrane bending moduli using light sheet fluorescence imaging of vesicle fluctuations. *Langmuir* **2013**, 29, 14588-14594.

Loftus, A.F.; Hsieh, V.; Parthasarathy, R., Modulation of membrane rigidity by the human vesicle trafficking proteins Sar1A and Sar1B. *Biochemical and Biophysical Research Communications* **2012**, 426, 585-589.

Settles, I.; Loftus, A.F.; McKeown, A.N.; Parthasarathy, R., The vesicle trafficking protein Sar1 lowers membrane rigidity. *Biophysical Journal* **2010**, 99, 1539-1545.

Andrew F. Loftus, Katey Reighard, Susu Kapourales and Michael C. Leopold. Monolayer-Protected Nanoparticle Film Assemblies as Platforms for Controlling Interfacial and Adsorption Properties in Protein Monolayer Electrochemistry. *Journal of American Chemical Society* **2008**, 130, 1649-61.

D. J. Tognarelli, Robert B. Miller, Rebecca R. Pompano, Andrew F. Loftus, Daniel J. Sheibley, and Michael C. Leopold. Covalently Networked Monolayer-Protected Nanoparticle Films. *Langmuir* **2005,** 21, 11119.

ACKNOWLEDGMENTS

I wish to thank a number of people for help, not only during the writing of this manuscript, but throughout my time at the University of Oregon. First and foremost I want to thank Professor Raghuveer Parthasarathy for allowing me to join his lab, mentoring me throughout my graduate school career, and taking a chance on a chemist who once believed physics was too painful a subject to even approach. Additionally, I would like to thank the Remington Laboratory, especially Karen Kallio, for help with protein purification, Stacey Smith and Jamie Purcell from the Berglund lab with HPLC purification and bacterial cloning, and the Nolen Lab for use of instruments. Special thanks goes to Tristan Hormel, Mike Taormina and Matt Jemielita for helping with editing of the manuscript as well as putting up with me in lab over the last 4 to 5 years! Thanks to Vivian Hsieh and Sigrid Noreng for help on experimental work on the projects over the years and my committee for their input throughout my candidacy. Furthermore, I could not have survived this arduous process without my friends and family to keep me motivated and being there when things were tough. A special thanks to Allison Hollinger, who was always up for a late night call and a calming factor when things were hectic. Finally, I would like to thank Professor Mark Lonergan for helping me early in graduate school with going outside my comfort zone with my work.

I dedicate this dissertation to my Mother, Father and Three Brothers: Patrick, Matthew and Mark

TABLE OF CONTENTS

Chapter Page

Chapter Page

LIST OF FIGURES

Figure Page

LIST OF TABLES

Table Page

CHAPTER I

INTRODUCTION

Bilayer lipid membranes play key roles in numerous functions in all organisms. They are composed of two leaflets, each consisting of individual lipids having hydrophobic carbon chains and hydrophilic head groups. Leaflets slightly interdigitate their hydrophobic carbon chains, exposing hydrophilic lipid headgroups to the surrounding environment creating bilayer lipid membrane barriers. Lipid bilayers can be considered quasi-two-dimensional materials roughly 5 nm thick, able to bend and create curvature in three-dimensional space. The ability to perform these manipulations allows for essential functions in the deployment of neurotransmitters[1], movement of cells[2] and the ability to transport cellular cargo.[3] Essential characteristics of the functions stated above are the ability to deform membranes and control curvature. Families of proteins will often associate with the membrane, creating scaffolds on or near the membrane surface to alter curvature.[4] Recent research associated with membrane curvature focuses primarily on the proteins whose structure shapes curvature and the biochemical interactions between these proteins.[5-8] How specific proteins modulate force and energy to sculpt membranes is still under investigation. Understanding how proteins play a role in membrane curvature will provide greater insight into the mechanics of curvature generation and help determine the capabilities of proteins in the dynamic process of vesicle trafficking, a fundamental process by which cells transport intra- and intercellular cargo.

Proteins involved in vesicle trafficking must bind to and bend membranes, creating highly curved forms that are subsequently constricted at a neck, pinched off, and transported to their destinations along with encapsulated cargo. Existing mechanistic views of transport vesicle formation have focused largely on the creation of scaffolds by rigid macromolecular assemblies. Proteins such as clathrin[6], Bin-Amphiphysin-Rvs (BAR) domains[5,7] and Sec 13 and 31[8] contain geometrically curved motifs to sculpt the membrane. The protein-mediated alteration of underlying, geometry-independent, membrane material properties such as rigidity, however, has been overlooked, even though lipid membrane mechanics are key determinants for curvature generation.[2,3,9-12] Creating the shapes necessary for transport vesicles is energetically unfavorable, possessing a barrier that must be overcome to create the curved vesicle bud. In order to manipulate the geometry of the membrane, it is plausible that reductions in membrane rigidity and tension could be used to overcome this barrier. Proteins associated with the membrane could be capable of performing these manipulations and such a protein is the primary focus of this work.

Transporting essential membrane and lumenal cargo proteins synthesized at the endoplasmic reticulum (ER) for the secretory pathways of the cell requires generation of curved buds formed into vesicles from the ER membrane (Figure 1). The coat protein II (COPII) complex consists of five proteins necessary for the formation of vesicles at the ER.[13,14] Sar1, a relatively small, 21.5 kDa G-protein of the Ras superfamily, binds directly to the ER lipid bilayer membrane and is the only member of the COPII family to do so. Sar1 associates with the membrane via an N-terminal amphipathic alpha helix.[15,16] Sar1's association with the guanosine triphosphate (GTP) nucleotide produces an active

state by exposing the N-terminal helix for association with the membrane. Sar1 then recruits the dimeric cargo adaptor, Sec23/24 complex. Sec23 modulates the GTPase hydrolysis of Sar1 by contributing essential residues for the activation of hydrolysis[17], while Sec24 interacts with cystolic tails of transmembrane proteins in the association of cargo and recognizes a diverse protein array on the ER to selectively recruit cargo.[18] The complex of Sar1-Sec23/24 creates the prebud complex of proteins. Finally, the prebud complex recruits Sec13/31, a tetraheteromeric complex to the membrane. Sec31 further drives GTPase activity by optimizing Sec23's amino acid positions to hydrolyze bound GTP.[17,19,20] Sec31 further provides structural support to the clathrate cage formed around the budding vesicle in coordination with Sec13. Sec13 in turn provides the force required for the shape changes in the underlying membrane into a vesicle form. The vesicle is then capable of pinching off the ER membrane, following which it is transported by the cytoskeleton components of the cell to the Golgi apparatus.

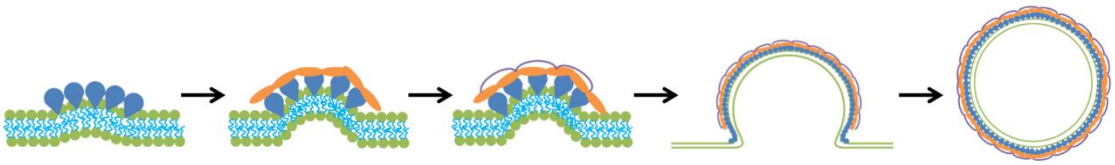

Figure 1. Schematic representation of vesicle membrane formation.

Sar1 binds to GTP with support from Sec12, an integral guanine exchange factor (GEF) protein excluded from the COPII vesicle system that plays an important role in the exchange of GTP into the binding pocket of Sar1.[21] The exchange of GTP in Sar1 results in a structural rearrangement of the protein, most notably in the N-terminal amphipathic alpha helix (Figure 2A). The helix insertion into the ER membrane allows for the hydrophobic hemi-cylinder (Figure 2B) of the helix to interact with the hydrophobic

hydrocarbon tails of the outer leaflet while charged residues of the helix face interact with hydrophilic headgroups of the membrane. The recruitment of the Sec23/24 prebud complex then interacts with Sar1 and subsequent steps for vesicle trafficking as stated earlier are performed.

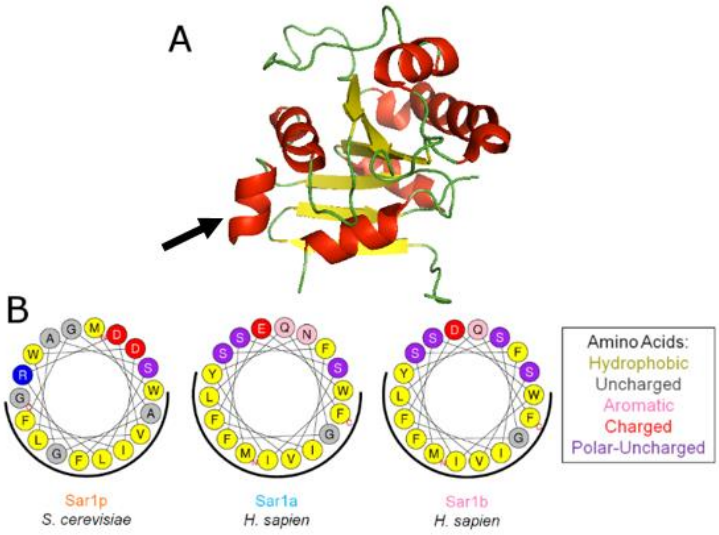

Figure 2. Sar1 crystal structure and helical wheel plots. Sar1B-GDP open conformation crystal structure and helical wheel plots of N-terminal alpha helices for Sar1p, Sar1A and Sar1B. (A) Sar1B-GDP crystal structure at low magnesium concentrations revealing the open conformation of the protein at 1.82 Å resolution, structure created in PyMol® (PDB ID: 2FMX).[22] The arrow is pointing to the partial N-terminal alpha helix resolved in the structure. (B) Helical wheel plots of the N-terminal amino acids of Sar1 proteins. Each Sar1 has a distinctive hydrophobic hull (black arc) with charged residues on the opposite face, enabling association with lipid bilayers.

Between different organisms the number of Sar1 proteins involved in vesicle transport varies. The yeast, *Saccharomyce cerevisiae*, contains only one copy of Sar1 (Sar1p), while mammals have two paralogs, denoted Sar1A and Sar1B. All three Sar1s have similar secondary structures[23-25] and possess an N-terminal amphipathic alpha helix (Figure 2B). Sar1A and Sar1B both perform trafficking from the ER to the Golgi, but there are some distinct differences between the two paralogs. Sar1B has a role in

transporting larger cargo in the form of chylomicrons (60-80 nm vesicles) compared to Sar1A.[26] Due to this difference in cargo trafficking, Sar1B may have a role in adapting the COPII coat to accommodate larger cargo[27] that may point to differences in the modulation of bending rigidity between the two human proteins. Interestingly, rare fat adsorption disorders involving transport of large lipid capsules are associated with defects in Sar1B but not Sar1A.[28] This could be a difference in mechanics between mammalian Sar1s in manipulating the membrane for specific cargo. The variation in membrane trafficking leads to questions of how the mechanics of the protein in both yeast and mammalian Sar1's create changes in the membrane.

Sar1p with bound GTP or nonhydrolyzable GTP analogs has been reported to generate curvature and tubulation *in vitro* from liposomes of sizes ~20-300 nm in diameter with lipid composition mimicking that of the ER, as visualized with electron microscopy.[15,16] Additionally, the amphipathic alpha helix of the protein was removed and replaced with a hexahistidine amino acid sequence to further determine the necessity of the N-terminal alpha helix.[15,16] Utilizing chelated Ni-lipids as binding sites the Sar1p-hexahistidine (Δ23-Sar1p) bound efficiently to the membrane, but did not show any of the same deformations seen with the full length protein.[15] With addition of Sec23/24 proteins pre-bud protein formations were created with Δ23-Sar1p, but vesicles were never released from the liposomes.[15] This evidence reveals Sar1 is more than an anchor for the rest of the COPII proteins to associate with, implying a scenario where the importance of the helix is significant to the ability to create deformations and ultimately traffic vesicles.

The mechanics of Sar1 are inadequately explained, leaving a void in the understanding of the overall function of Sar1 and the result it has on the physical characteristics of the membrane. Prior to our work, the prevailing hypothesis predicted Sar1 generates curvature in the context of the bilayer couple mechanism: Sar1's N-terminal helix inserts into the membrane's outer leaflet increasing surface area in comparison to the inner leaflet of the membrane.[29,30] Expansion of the outer leaflet area creates a force altering the geometric shape of the membrane leading to deformations and tubulations. Expansions from insertions, especially pronounced in systems where the constraint of a small-bounded volumes, means that a small asymmetry in leaflet areas leads to significant deviations in spherical shape. When creating local deformations on relatively large surface areas such as the ER, however, it is difficult to envision how the bilayer couple mechanism produces local curvature with global contributions, as specific regions of the membrane direct Sar1 for association creating local deformations.

We approach this problem by hypothesizing that Sar1 alters the energetic cost of curvature in the ER membrane. Proteins can lower this energetic cost by lowering the bending modulus (i.e. rigidity, κ), an intrinsic material property of lipid bilayers which determines the energetic cost of curvature.[2,3,11] Modulating the reduction in rigidity results in a more flexible and moldable membrane, capable of being structured into a budding vesicle by the proteins of the COPII complex. This mechanism provides the capability to localize rigidity minimization for the creation of vesicles necessary for transport.

In order to test our hypothesis we need the ability to directly determine the force of deformation, which yields the bending modulus of membranes and measure the impact

Sar1 has when binding to the membrane. The approaches we take to explore this are twofold: utilizing an optical trapping technique and measuring thermal fluctuations of vesicles *in vitro* to measure the physical properties of artificial ER-mimic membranes.

Optical trapping techniques were first developed in the early 1970s revealing that optical forces could displace micron-sized dielectric particles in water and air.[31] Optical traps generate force by focusing light through the objective of a microscope, which (for suitable materials) creates a potential well at the focal point. Since its invention, trapping has been refined and utilized in multiple experimental setups, from manipulating bacteria[32] to trapping neutral atoms.[33] We utilize the optical trap to displace microspheres attached to membranes *in vitro* by pulling the bead away from the bulk membrane, creating cylindrical membrane tethers (Figure 3). We use this technique because the geometry and therefore mechanics of tethers are well known as described further in Chapter II. The total mechanical energy of a tether is the sum of several terms: the bending energy and coupling energy integrated over the cylinder area, the elastic energy as a product of the tension and cylinder area and the mechanical work as a product of the force of extension and the length of the tether.[34-39] Blocking the trap allows the tether to retract, and we are able to observe the velocity of the retraction and thus measure the force of the membrane to the bulk reservoir. Elucidating the rigidity of tethers is possible by measurement of the force and the tether radius.

Giant lipid vesicles, tens of microns in diameter, exhibit thermally driven undulations. With careful imaging and analysis, the magnitude and spectrum of the undulations can reveal the vesicle membrane rigidity. Since the 1980s, vesicle fluctuations have been used to determine the rigidity of membranes and improvements to

the technique have been developed throughout the last 30 years.[40-42] To improve this method we have performed light sheet observations, showing usefulness as an alternate method and possibly higher throughput than our tether pulling assay. This again reveals membrane rigidity changes induced by Sar1, and helps address the large spread in lipid-only membrane rigidity values.[40-41,43-48]

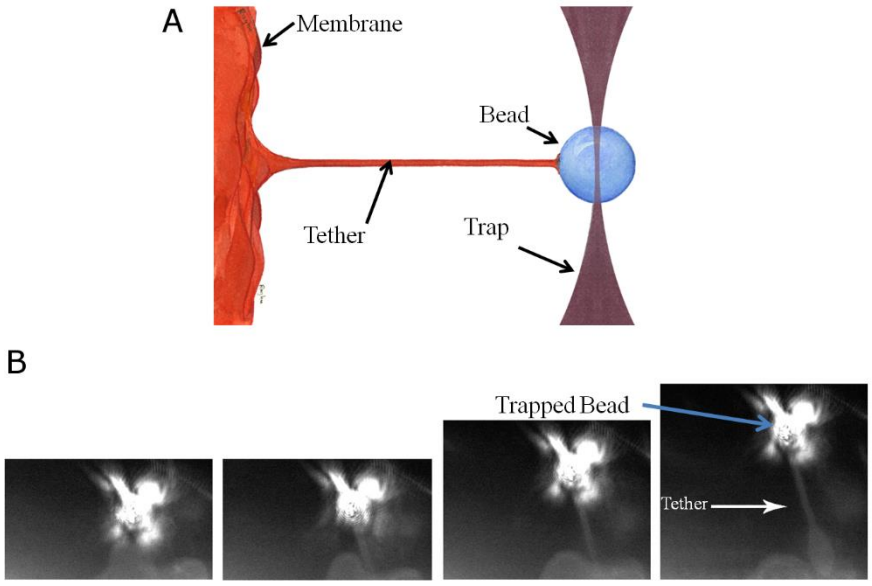

Figure 3. Tether pulling assay. (A) Schematic of tether pulling experiment. Pulling a membrane-anchored microsphere with an optical trap generates a cylindrical membrane tether. Upon release of the microsphere, the tether retracts to lower its curvature-associated mechanical energy. (B) From left to right a bead trapped in the focused laser pulled away from the membrane creating a tubule of membrane.

Finally, I discuss our progress towards making a minimalistic system to create bioconjugated mimics to produce results we see with Sar1p at high concentrations. We have attempted to use synthetic peptides of the amphipathic alpha helix of Sar1p and a bioconjugation technique to create a multi-helical scaffold.[49] A scaffold of the helices we hope mimics the natural COPII coats' cross-linking of multiple Sar1 proteins via the other coat proteins. Our attempts to create such a scaffold have been unsuccessful to date,

but we continue our effort in striving for a functional peptide scaffold. I provide insight for future work that the project can utilize to move forward and I provide discussion on this topic.

Chapter II provides detailed information towards our understanding of how mammalian and yeast Sar1 effect the overall rigidity of the ER membrane and its relation to the trafficking of cargo in cells. The work pertaining to Sar1p and Δ23-Sar1p was previously published in volume 99, September 2010 in *Biophysical Journal* with co-authors Edward I. Settles, Alesia N. McKeown and Raghuveer Parthasarathy and studies involving Sar1p, Sar1A and Sar1B were previously published in volume 426, September 2012 in *Biochemical and Biophysical Research Communications* with co-authors Vivian L. Hsieh and Raghuveer Parthasarathy. Chapter III provides detailed information on the work we put forth on thermal vesicle fluctuation measurements. This work was previously published in volume 29 in *Langmuir* November 2013 with co-authors Sigrid Noreng, Vivian L. Hsieh and Raghuveer Parthasarathy. Chapter IV will discuss our progress towards the creation of a simple synthetic model for reducing rigidity and understanding the amphipathic alpha helix. The conjugation protocol was provided by David Rabuka of Redwood Biosciences. Alex MacLeod and Vivian L. Hsieh contributed to preliminary work and Raghuveer Parthasarathy provided insight into ideas and focus for the work.

CHAPTER II

THE VESICLE TRAFFICKING PROTEIN SAR1'S MODULATION OF MEMBRANE RIGIDITY

Reproduced with permission from Settles, E.I., Loftus A.F., McKeown, A.N. and Parthasarathy R. *Biophysical Journal* 99: 1539-1545. Copyright 2010, Biophysical Journal.

Reproduced with permission from Loftus, A.F., Hsieh, V. and Parthasarathy R. *Biochemical and Biophysical Research Communications* 426: 585-89. Copyright 2012, Biochemical and Biophysical Research Communications.

Control of membrane curvature is critical in many cellular contexts, in particular the construction of transport vesicles that traffic cargo between membranous organelles.[2,3,11] Many of the proteins associated with curvature have been identified and a large and growing body of knowledge describes their structures and biochemical interactions. Much less is known, however, about the mechanics of curvature generation: how specific proteins modulate forces and energies to sculpt intracellular membranes into dynamic, curved forms. As discussed in Chapter I, existing mechanistic views of transport vesicle formation have focused largely on the creation of scaffolds by rigid macromolecular assemblies. The possibility of protein modulated membrane material properties such as rigidity, however, has been neglected, although lipid membrane mechanics are a key determinant of the energetic cost of curvature generation and can couple to protein structures in a wide variety of ways.[2,3,9,10,12]

Sar1, a small GTPase (21.5 kDa) protein of the COP II family has demonstrated the ability to deform liposomes absent of the other COP II components as described in Chapter I.[15, 29] While Sar1 may employ the bilayer couple mechanism discussed earlier, explorations of other mechanisms, which need not be mutually exclusive, are warranted. It has remained unknown, however, whether Sar1 proteins lower membrane rigidity at all, and if so, whether they do so in a similar manner between homologs of Sar1. We therefore measured the rigidity of lipid bilayer membranes as a function of Sar1A, Sar1B, and Sar1p concentration.

EXPERIMENTAL DESIGN

We hypothesized that Sar1's helix insertion alters the material character of the membrane, specifically its bending modulus (or rigidity, κ), which determines the energetic cost of curvature.[2,3,11] We measured rigidity and its modulation by Sar1 using a membrane tether-pulling assay that recapitulates relevant aspects of ER morphology in an *in vitro* setting. In both cell-free and live-cell contexts, membrane deformation by an external unidirectional force can draw out cylindrical membrane tethers (Figure 2 and Figure 4).[34,35,38,50]

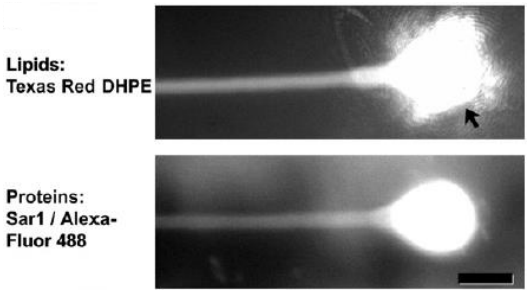

Figure 4. A membrane tether, pulled by an optically trapped bead. (Top) Fluorescence image of Texas Red DHPE labeling the lipid membrane. (Arrow) Bead and the trapping laser light. (Bottom) Fluorescence image of Alexa Fluor 488-labeled Sar1p from the same tether. (Bar) 10 μm.

Tether mechanics are well understood: the mechanical energy associated with the one dimensional curvature of a tether of radius *R* and length *L* is proportional to the tether area and hence to the product *RL*, giving rise to a length-independent contractile force, *f*. Measurement of both *f* and *R* reveals the membrane rigidity; a derivation is provided in Appendix A. In brief: the bending energy per unit area of a membrane, ε, is a function of the local principle radii of curvature (R_1 and R_2), the bending modulus, κ, the Gaussian curvature modulus (κ_G), and the spontaneous curvature (c_0)[51,52]:

$$\varepsilon = \left[\frac{\kappa}{2}(R_1^{-1} + R_2^{-1} - 2c_0)^2\right] + \kappa_G R_1^{-1} R_2^{-1}. \quad \text{(Eq.1)}$$

The spontaneous curvature, at which the bracketed term is minimal, gives the geometry of the lowest energy configuration of the unperturbed membrane. For lipid bilayers with identical leaflet composition, $c_0 = 0$.[2,3] Membrane inclusions, such as inserted proteins, can change the membrane rigidity directly by altering κ (e.g., by altering lipid packing or thinning the membrane)[9,35,38,53,54], or indirectly by coupling to the local curvature and reducing the effective rigidity with respect to deformations.[10] The curvature-mediated interaction can be accounted for by an additional energetic term proportional to the local curvature $c = R_1^{-1} + R_2^{-1}$, the inclusion density ϕ, and a coupling constant, Λ. (Additional terms describing self-interactions among inclusions are described in Appendix A.) For a membrane tether of radius *R*, $R_1 = R$ and $R_2 = \infty$, the total mechanical energy, *E*, is the sum of contributions from the bending energy, the inclusion-curvature coupling, the elastic energy given by the product of the tether area and the membrane tension, σ, and the mechanical work given by the product of *f* and *L*. Minimizing *E*, it follows that

$$\frac{fR}{2\pi} = \kappa - \Lambda\phi R. \quad \text{(Eq.2)}$$

The functional relationship between the measurable force and radius values reveals κ and $\Lambda\phi$. In the absence of coupling between the inclusions and the local curvature (i.e., $\Lambda = 0$), $fR = 2\pi\kappa_0$; we will denote the rigidity in this case, in which the role ascribed to the proteins is to directly alter membrane rigidity, as

$$\kappa_0 = fR(2\pi)^{-1}. \quad \text{(Eq.3)}$$

The tether energy function can also be analyzed to provide σ_0, a measure of the sum of the membrane tension and the (indistinguishable) interaction energy of the proteins; details are provided in the derivation provided in Appendix A.

We created, deformed, and mechanically characterized lipid membranes incubated with varying concentrations of Sar1. Details of compositions and procedures are given in Materials and Methods. In brief: lipid films of the desired compositions were dried on glass coverslips and hydrated in HKM buffer. The resulting multilayer lipid bilayer sheets had a large surface area (~ 10^6 μm^2), like the ER and unlike liposomes. Again, in contrast to liposomes, the lack of strong geometric constraints on area enables low tension in our system.[55] As in earlier liposome-based studies, we used lipid compositions rich in phosphoethanolamine and phosphatidylinositol lipids.[15,56] A small fraction of fluorescent-labeled lipids allowed membrane visualization by fluorescence microscopy. Lipids with biotin-conjugated headgroups allowed binding of ~5 μm diameter streptavidin-coated polystyrene beads that served as anchors for tether pulling. Membranes were incubated with Sar1, EDTA, and the nonhydrolyzable GTP analog GMPPNP.[15,56]

After incubation with streptavidin-coated beads, individual microspheres were manipulated manually using a home-built optical trap[31,57-58] to pull a membrane tether

tens or hundreds of microns in length. The tether is pulled parallel to the substrate, beyond the edge of the hydrated membrane sheets, and is therefore clearly visible against the lipid-free coverslip background. The trap was then turned off, leading to immediate retraction of the tether, dragging the bead with it; retraction lowers the area of curved membrane and the associated bending energy. The beads were imaged and tracked via high-speed video microscopy, yielding the tether speed, *v*. The tether force, *f*, equilibrates with the drag force on the bead, *bv*. The drag coefficient, *b*, was experimentally determined for each tether by analyzing the probability distribution of position fluctuations of the bead described further in Materials and Methods.[59] This approach provides drag coefficient, *b*, independent of the nature of dissipation in the system, which may be a combination of hydrodynamic drag of the bead through the surrounding fluid or viscosity within the lipid bilayer.[60] The tethered bead trajectory reveals the tether force ($f = bv$). Notably, this approach is intrinsically insensitive to properties of the optical trap, being applied when the trap is off and relying only on fundamental statistical mechanical behaviors to quantify forces.[59] Tether radii were measured from fluorescence images taken before the retraction of the pulled tether.

MATERIALS AND METHODS

Lipid membranes were composed of the Major Mix mixture as in Matsuoka et al.[14] mimicking the composition of the ER membrane. The composition is modified to include fluorescent probes and biotinylated lipids: 51.5 mol % DOPC (1,2-dioleoyl-sn-glycero-3-phosphocholine), 23.0 mol % DOPE (1,2-di-(9Z-octadecenoyl)-*sn*-glycero-3-phosphoethanolamine), 11.0 mol % PI (L-α-phosphatidylinositol, from Soy), 8.0 mol % DOPS (1,2-diacyl-*sn*-glycero-3-phosphoserine), 5.0 mol % DOPA (1,2-di-(9Z-

octadecenoyl)- *sn*-glycero-3-phosphate), 0.5 mol % Texas Red DHPE (Texas Red 1,2-dihexadecanoyl-sn-glycero-3-phosphoethanolamine), and 1.0 mol % biotinyl-cap-PE (1,2-dihexadecanoyl-*sn*-glycero-3-phosphoethanolamine-N-(cap biotinyl)). For experiments involving hexahistidine-terminated Δ23-Sar1p, the membrane included 5 mol % nickel-chelating lipids (DOGS-NTA-Ni,1,2-di-(9Z-octadecenoyl)-*sn*-glycero-3-[(N-(5-amino-1-carboxypentyl) iminodiacetic acid)succinyl] (nickel salt)), with other lipid fractions proportionally rescaled. All lipids were purchased from Avanti Polar Lipids, except Texas Red DHPE, which was purchased from Life Technologies.

Sar1 expression

Protein expression was performed with a PTY40 expression vector (a pGEX-2T backbone (GE Healthcare) with inserted glutathione S-transferase strain RSB245410 (Sar1p), RSB3771 (Sar1A) or RSB3772 (Sar1B) or a hexahistidine Δ23-Sar1p insert in BL21 bacterial expression cells (UC Berkeley, Schekman Group). Proteins were expressed and purified using protocols modified from Ref. [15]. In brief, cells were grown in 4 L 2x YT broth to an OD_{600} = 0.2-0.3 at 37 °C. Further growth to an OD_{600} = 0.7-0.8 at 25 °C was then induced with 0.1 mM IPTG for 1h. Cells were pelleted at 5000 rpm in a Ka 9.1 Rotor (Kompsin) for 25 min. and suspended in 20 mL of TBST (50mM Tris, 150mM NaCl, 0.1 % Tween-20®, pH= 7.4) with the addition of 0.5 mL of a 40 mg/mL lysosyme solution on ice for 20 minutes. Triton-X 100 was then added to 1 % to the suspension. The cell suspension was then sonicated with a Sonic Dismembrator Model 500 (Fisher Scientific) with pulses of 30 s each, 3 times. The suspension was centrifuged at 15000 rpm in a JA-20 (Beckman) rotor for 20 m with the supernatant transferred to a 50 mL Falcon tube. 8 ml of a 50 % Glutathione Sepharose 4B slurry (GE

Healthcare) was washed in TBST 3 times and the beads were transferred to the supernatant tube. The supernatant slurry was incubated for 1 h. at 4 °C with slow rotation and spun down at 5000 rpm for 5 min. in a JA-20 with the supernatant poured off. The beads were then washed subsequently 3 times in TBST, 2 times in TBS (50 mM Tris, 150 mM NaCl, pH = 7.4), and once in TCB (50 mM Tris, 250 mM KoAc, 5 mM $CaCl_2$, pH= 8.0) each time being spun down at 5000 rpm for 5 min. in a JA-20 rotor. The beads were transferred to a 10 cc miniprep column and incubated with thrombin (4U) for 90 min. The protein was then eluted with TCB and buffer exchanged using a PD-10 column with HKM (20 mM Hepes, 160 mM KoAc, 1mM $MgCl_2$, pH=7.0). The collected fractions were then stored at -80 °C. For the small fraction of experiments involving visualization of Sar1p, proteins were labeled at primary amines with Alexa Fluor 488 fluorophores (Alexa Fluor 488 Microscale Protein Labeling Kit, Life Technologies). For control experiments on the mechanical influence of a hexahistidine tag, synthetic fluorescein-conjugated his-6 was purchased from Biomatik. (The fluorescein enabled verification of membrane binding.)

Sample preparation

5 µL of Major Mix was vacuum dried on the bottom of an 8-well incubation chamber (Fisher Scientific). Dried lipid films were then hydrated with 0.2 ml HKM buffer (20 mM HEPES-KOH, pH 6.8, 160 mM potassium acetate, 1 mM $MgCl_2$) yielding multilayered membrane stacks. Sar1 (A, B or p) or Δ23-Sar1, 100 mM GMPPNP (Sigma-Aldrich, St. Louis, MO) and 4 mM EDTA were incubated together in an Eppendorf tube for 5 min., after which they were added to the chamber containing membranes and buffer. Nucleotide uptake by Sar1 was verified by tryptophan fluorescence experiments (See

Appendix A and Appendix B for details).[20,61] After ~5 min, a few microliters of a suspension of ~5 μm diameter streptavidin-coated silica microspheres (Bangs Laboratories, Fishers, IN) were added to the chamber. Appendix A has further method details available.

Optical trapping and particle tracking

Microspheres were trapped with a home-built optical trap setup using a 671-nm, 120-mW diode laser (model No. RS71-100PS; Meshtel, AKA Intelite, Genoa, NV). Microsphere images were captured with bright-field microscopy using a Model No. pco.1200 camera (Cooke, Romulus, MI) at 100 frames per sec. Particle positions were determined using home-built tracking software that employs well-established algorithms[62,63] with ~10 nm precision.

Particle positions were determined using home-built tracking software. Hough transformation of ring-like bright field particle images yielded peaks whose centers were determined by nonlinear fitting of two-dimensional Gaussian functions. Tracking test particles stuck to glass coverslips, with the same exposure and illumination settings, shows a localization precision of 5 nm (0.02 px), as would be expected[16] for images with a signal-to-noise ratio of ≈ 100. The drag coefficient is determined from velocity fluctuations for each tether independently following the general approach described by Sainis et al.[59] The uncertainty in b due to tracking precision is approximately 1 %, and so is negligible compared to the statistical variability of tether data. Alternatively localizing particles by fitting ring-like particle images directly using a radial-symmetry-based fitting[16], without the intermediate step of Hough transformation, yields indistinguishable results.

Drag coefficient

The drag coefficient is determined independently for each tethered microsphere following the general technique described in REF. [39]. The microsphere position (x) is well described by a constant velocity (v) retraction together with random (Brownian) motion about this linear drift. The probability distribution of step sizes (Δx) between frames separated in time by Δt therefore follows a Gaussian form:

$$P(\Delta x) = (2\pi\gamma^2)^{-\frac{1}{2}}\exp[-(\Delta x - \langle\Delta x\rangle)^2/(2\gamma^2)]. \quad \text{(Eq.4)}$$

Where the mean step size $\langle\Delta x\rangle = v\Delta t$ and the width, γ, is related to b via the Einstein-Smoluchowski relation: $\gamma^2 = 2k_B T(\Delta t)b^{-1}$, where k_B is Boltzmann's constant and T is the absolute temperature. Analyzing $P(\Delta x)$ therefore reveals the drag coefficient. Notably, this approach determines b for the tether-plus-microsphere system independent of assumptions about the nature of the dissipation in the system.

Tether images and radii determination

Fluorescence images of membrane tethers were captured with an ORCA-ER charge-coupled device camera (Hamamatsu, Hamamatsu City, Japan). Tether radii were determined from Texas Red DHPE fluorescence images by measuring the intensity along lines perpendicular to the tether axis, averaged over approximately 1 μm along the tether length. We estimated the uncertainty in optical determination of the tether width by calculating the intensity profiles with the observed data. Even for the narrowest tethers (R = 200-300 nm, ~7 % of the tethers) the correction to the radius values associated with diffraction-limited resolution was at most 10 %, and hence is negligible compared to the statistical scatter. For tethers of radii over 300 nm (93 % of data), the radius correction due to diffraction is less than 1 %. Peristatic fluctuations of tethers[64] i.e. wiggles from the

equilibrium center of mass configuration, are slower by over two orders of magnitude than the exposure times used in fluorescence imaging, and hence due not hinder determination of tether radii.

Fluorescence imaging for binding affinities

Sar1 proteins were prepared and incubated with Major Mix membranes in the same manner as described above, but with the non-hydrolyzable nucleotide, GMPPNP replaced by the fluorescent BODIPY FL GTP-γ-S (BD-GTP-γ-S, Life Technologies) to visualize the Sar1 bound to membranes. Gentle washing with protein-free HKM buffer was performed to remove excess BD-GTP-γ-S and unbound protein. Fluorescence images were taken of both Sar1-BD-GTP-γ-S and Texas Red-DHPE with the ORCA-ER CCD camera. Intensity values and background subtraction were performed using in-house software written in MATLAB (MATHworks).

Electrostatic calculations

Electrostatic potential maps for Sar1 lacking the terminal helix were calculated using PBEQ-Solver[65] applied to the structure from Bi et al.[23] (PDB ID 1M2O) and visualized with PyMol® (http://www.pymol.org/).

Membrane and protein diffusion determination

Protein and lipid mobility were measured by examining fluorescence recovery after photobleaching (FRAP).[66] For each measurement fluorescent probes were bleached for 2 to 3 seconds with a 473 nm, 50mW diode laser (DHOM Model number: DHL25A, Ultralasers) focused to a spot. Images were acquired at discrete time points after bleaching and analyzed to determine the diffusion coefficients by modeling fluorescence recovery as a two-dimensional random walk.[67] In brief, we determine the diffusion

coefficient that generates the best-fit match between a time-evolved initial image and a measured final image, an approach that requires no assumptions about the size or shape of the bleached spot.

RESULTS

Sar1p rigidity measurements

We first explored Sar1p. Upon the release of the bead from the optical trap, the tethers exhibited a constant-velocity regime of bead retraction, indicating a constant, length-independent tether force as expected. Fluorescence images of a tether are shown in Figure 4. The mean R was 0.6 μm with a standard deviation (SD) of 0.2 μm for >700 tethers examined (see Materials and Methods for details of the radius determination). Three representative trajectories from tethers with similar radii are plotted in Figure 5, with 0, 0.373, and 3.73 μM Sar1p-GMPPNP, [Sar1p], the final value being similar to the concentration employed in liposomes deformation assays.[15] At long times after release, the microsphere velocities often slowed; one would expect the bead trajectory to be nontrivially related to the flexible tether's Brownian dynamics. We therefore focus on the initial constant velocity regime, in which the trajectory and the tether mechanics are simply related as described above. For the hundreds of tethers examined, the mean drag coefficient was $b = 0.125 \pm 0.064$ μN s/m, approximately three times the Stokes drag of a 4.8 μm diameter bead in an infinite three-dimensional aqueous space. The drag coefficient shows a slight rise as a function of [Sar1p] that may indicate the protein increases the interleaflet viscosity (Figure 6).

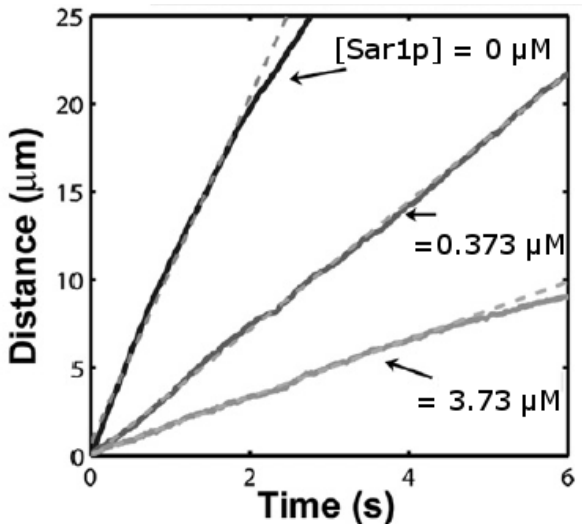

Figure 5. Tether retraction. The bead position after its release from the optical trap is plotted for three representative tethers of similar radii (R = 0.45-0.55 μm) and microsphere drag coefficients (b = 0.07-0.11 μN s/m), in the presence or absence of [Sar1p]. (Dashed lines) Linear fits to the initial trajectory.

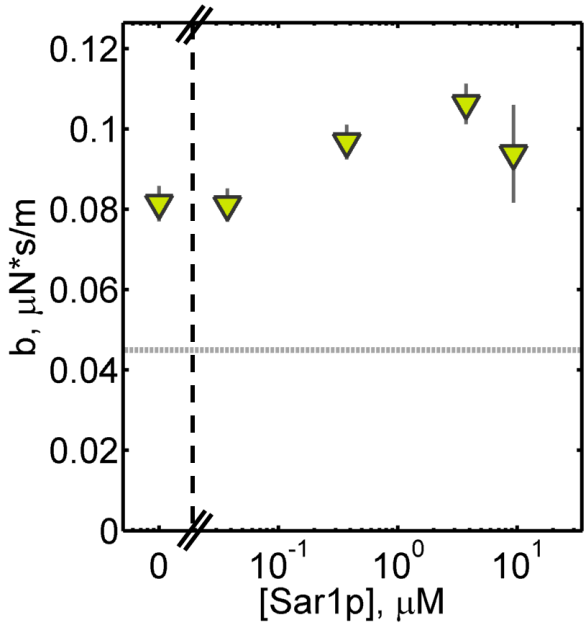

Figure 6. The measured drag coefficient, b, as a function of [Sar1p]. The dashed gray line indicates the Stokes drag of a 4.8 μm diameter sphere in an infinite extent of water. The black dashed line represents the broken x-axis.

We find that [Sar1p] lowers membrane rigidity in a concentration-dependent manner. In Figure 7A we plot κ_0 normalized by κ_{lipid}, the membrane rigidity in the

absence of protein, as a function of [Sar1p], showing a pronounced decline at both physiological and low ionic strengths (1X and 0.05X HKM, 180 and 9 mM, respectively). The values of κ_0, Table 1, are determined by averaging $fR(2\pi)^{-1}$ over all tethers pulled at a given protein and buffer concentration. This is by construction: κ_0 is precisely the rigidity if there is no curvature coupling, and hence if $fR(2\pi)^{-1}$ is independent of R. The more general case will be considered below.

At very high [Sar1p], ≈ 20 μM, we observed, in the absence of any optical manipulation, spontaneous disintegration of the membranes into liposomes or small tubules (Figure 7B; Video S1 Appendix B and the Supplemental Files included with this dissertation). This indicates that the curvature energy was smaller than the ambient thermal energy, implying that, roughly, $\kappa_0 < k_BT = 0.4 \times 10^{-20}$ J, where k_B is Boltzmann's constant and T is the absolute temperature. Tethers pulled in the absence of Sar1p, but with GMPPNP present at the same concentration as above, showed $\kappa_{lipid+GMPPNP} = (5.5 \pm 0.4) \times 10^{-20}$ J (N =49, 0.05X HKM). This is equal within uncertainties to the value for lipid-only membranes, $\kappa_{lipid} = (5.2 \pm 0.3) \times 10^{-20}$ J (N = 34, 0.05X HKM), indicating that nucleotide is not responsible for the membrane softening indicated in Figure 7A. The mean concentration of Sar1p in *S. cerevisiae* is roughly 0.23 μM, and so is spanned by the range of *in vitro* concentrations examined.[68]

We also compare mammalian Sar1-GMPPNP to Sar1p-GMPPNP as a function of [Sar1] (Figure 8). At low concentrations, the human proteins Sar1A and Sar1B also lower membrane rigidity, though by a lesser amount than Sar1p (Figure 8A). Strikingly, the rigidity of the membrane increases with concentration above 10 μM. Qualitatively, this high rigidity is evident from the integrity of tethers and membrane edges (Figure 8B-E).

Quantitatively, tether retraction measurements reveal the increase in κ_0, which is more pronounced for Sar1A than Sar1B (Figure 8A). Also plotted in Figure 8A and B are curves from a model that provides a possible functional form for the concentration dependence of κ_0, discussed later in the chapter.

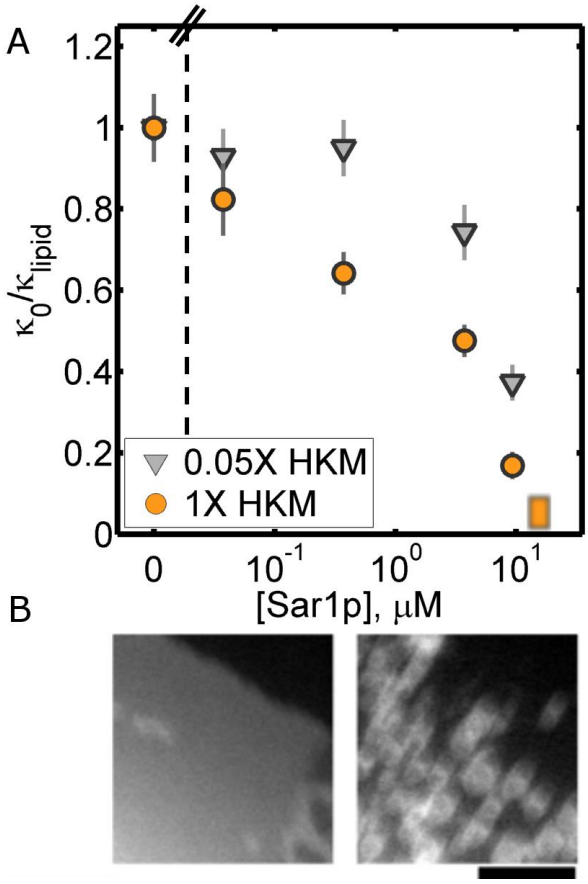

Figure 7. Measurement of rigidity as a function of [Sar1p]. (A) Membrane rigidity, κ_0/κ_{lipid}, as a function of [Sar1p]. Black dashed line represents a broken axis. The blurred box is drawn at a concentration at which spontaneous membrane disintegration is observed, indicating near-zero rigidity. (*Circles and triangles*) Data from experiments at 1X (180 mM) and 0.05X (9 mM) HKM buffer, respectively. (*Error Bars*) Standard errors of the means. (B) Spontaneous membrane disintegration. Fluorescence images of a region of membrane before (*left*) and after (*right*) the addition of [Sar1p] at ~20 μM. Scale bar = 10 μm.

Table 1. κ_0 values for Sar1p concentrations at 0.05X and 1X HKM buffer strength.

[Sar1p] μM	Number of Tethers	Buffer Strength	κ_0 (x10^{-20}J)
0	31	0.05X	5.2 ± 0.3*
0.04	19	0.05X	4.9 ± 0.4*
0.37	34	0.05X	5.1 ± 0.4*
3.73	33	0.05X	4.0 ± 0.4*
9.33	6	0.05X	2.0 ± 0.2*
0	9	1X	4.3 ± 0.3*
0.04	26	1X	3.5 ± 0.4*
0.37	12	1X	2.8 ± 0.2*
3.73	11	1X	2.1 ± 0.2*
9.33	6	1X	0.7 ± 0.1*

* The stated uncertainties are the standard errors of the means.

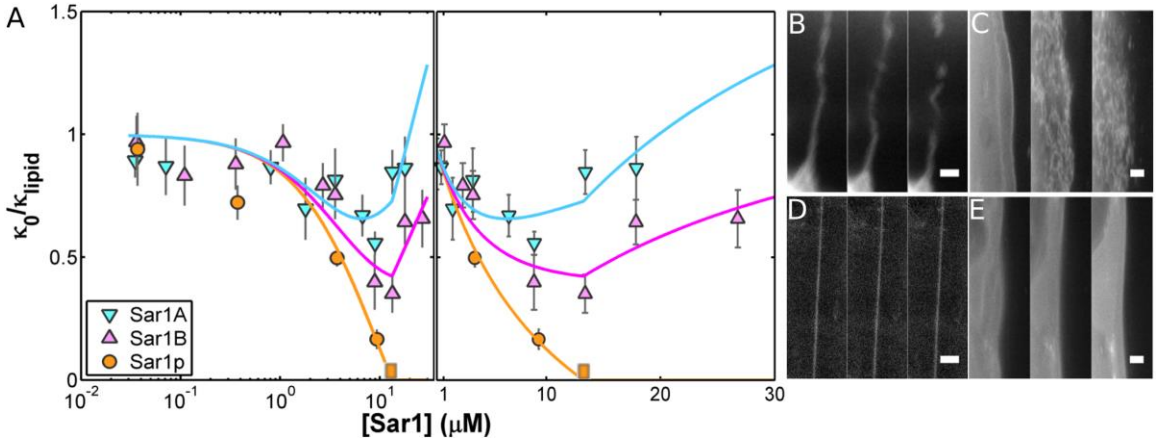

Figure 8. Comparison of Sar1 rigidity measurements. (A) Membrane rigidity as a function of [Sar1]. Curves indicate fits to the model discussed in the text. The left and right panels show the same data using logarithmic (*right*) and linear (*left*) concentrations axes, respectively. (B,C) Fluorescence images of Texas Red DHPE labeling lipid membranes in the presence of 20 μM Sar1p, depicting (B) a tether and (C) an unperturbed multilayer region of membrane. The three images in B and C are each separated by 15 s. (D, E) Lipid fluorescence images in the presence of 20 μM Sar1B, depicting (D) a tether and (E) an unperturbed multilayer region of membrane. The three images in D and E are each separated in time by 1 min. Scale Bars = 5 μm.

Curvature coupling

The reduction in κ_0 induced by Sar1, most pronounced in Sar1p, in principle could be due to a reduction in the true membrane rigidity, κ, or a positive value of Λ, i.e., an energetic preference for convex local curvature. Force measurements from tethers

spanning a range of radii allow separation of κ and $\Lambda\phi$ (Equation 2). We first apply this analysis to Sar1p lacking the N-terminal helix, denoted Δ23-Sar1p. As in Lee et al. the helix is replaced by a hexahistidine tag, enabling strong binding to membranes that include a small fraction (5 mol %) of nickel-chelating lipids.[15] (At solution concentrations of 3.73 μM, we find that Δ23-Sar1p binds membranes with a surface density ~2X greater than wild type Sar1p.) With Δ23-Sar1p, the product of *f* and *R* shows a linear dependence on *R* with a strongly positive slope (Figure 9), at 3.73 μM equivalence Δ23-Sar1p-GMPPNP, 0.05X HKM. This indicates a negative (concave) curvature coupling on the part of the protein, consistent with its inability to generate buds in liposome deformation experiments.[15] With 20 μM equivalence Δ23-Sar1p, we observe no spontaneous vesiculation of the membrane, in contrast to wild-type Sar1p, implying an energetic barrier to (convex) vesicle formation by the helix deleted protein. Neither the Ni-chelating lipids nor the hexahistidine tag in itself alters the membrane rigidity or induces significant curvature coupling: for protein-free membranes with Ni-chelating lipids, $\kappa_0 = (5.1 \pm 0.3) \times 10^{-20}$ J and $\Lambda\phi = -0.3 \pm 2.6$ J/μm (N = 30, 0.05X HKM), incubated with a hexahistidine peptide at molar concentrations equal to that of 3.73 μM Δ23-Sar1p, $\kappa_0 = (4.5 \pm 0.4) \times 10^{-20}$ J and $\Lambda\phi = -1.75 \pm 1.8$ J/μm (N = 17, 0.05X HKM). In contrast, Δ23-Sar1p gives $\Lambda\phi = -9.9 \pm 1.1$ J/μm.

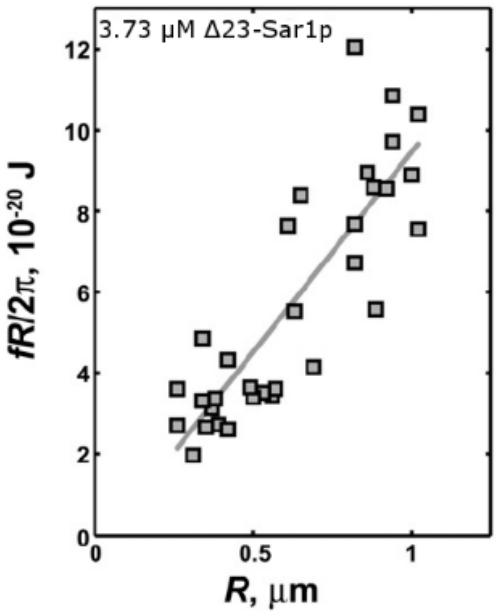

Figure 9. Δ23-Sar1p force versus radius fit. The product of the tether retraction force (*f*) and radius (*R*) plotted as a function of *R*, for 3.73 μM Δ23-Sar1p-GMPPNP, which lacks the amphipathic alpha helix of wild type Sar1. A positive slope indicates a negative coupling between the protein and the local curvature, or equivalently a concave effective spontaneous curvature.

Tethers formed with GMPPNP-bound wild-type Sar1p exhibit a much weaker dependence of *fR* on *R* (Figure 10A, 3.73 μM Sar1p, 0.05X HKM, 10B No Sar1p), and hence demonstrate little curvature coupling. Our studies of Sar1A and Sar1B show similar results for *fR* on *R* implying little curvature coupling of the mammalian Sar1s. This disproves the hypothesis that Sar1 imposes particular curvatures on the membranes to which it binds.[15] The magnitude of $\Lambda\phi$ is so small as to be barely resolvable, and shows a weak progression to increasingly negative values as a function of Sar1p concentration (Figure 11). The curvature coupling can be considered as an effective spontaneous curvature for the protein-bound membrane $c_0 = \Lambda\phi/(2\kappa)$, derived in Appendix A.[10] Throughout the range of [Sar1p] examined, the values of c_0 are negative and satisfy $|c_0| < 0.5\ \mu m^{-1}$. This corresponds to a preferred radius of curvature $R_0 = c_0^{-1} >$

2 μm, much larger than any of the characteristic dimensions of transport vesicles and hence unlikely to determine vesicle morphology. It follows from Λ (or c_{eff}) being negative that the true rigidity, κ, is smaller than κ_0 and the steep decline in κ_0 observed as a function of [Sar1p] (Figure 7A) reflects a reduction in κ. Moreover, the dependence of *fR* on *R* allows direct determination of κ (Equation 3). While subject to large uncertainties, κ shows the same sharp decline with [Sar1p] as does κ_0 (Figure 12). The membrane softening is similar at ionic strengths of 180 and 9 mM, corresponding to a factor-of-5 difference in Debye screening length.

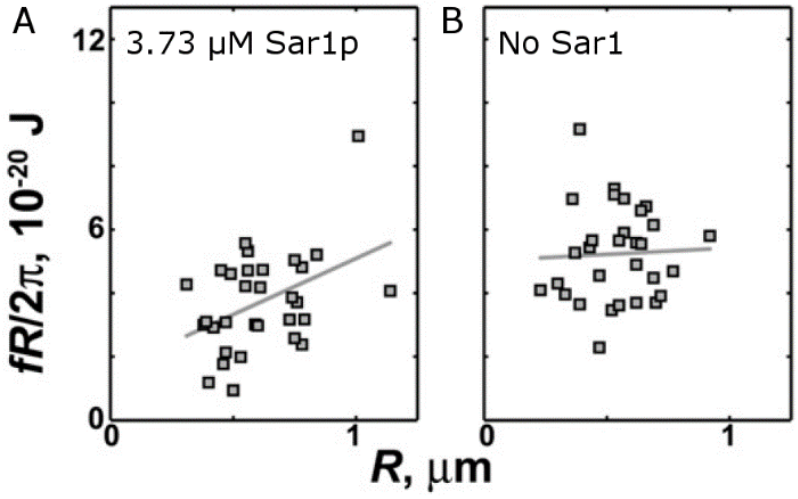

Figure 10. Sar1p and Major Mix force versus radius fits. (A) *f*R versus *R* for 3.73 μM Sar1p-GMPPNP and (B) *fR* versus *R* for membranes with no Sar1. The data plotted are from experiments in 0.05X HKM with linear fits (solid lines).

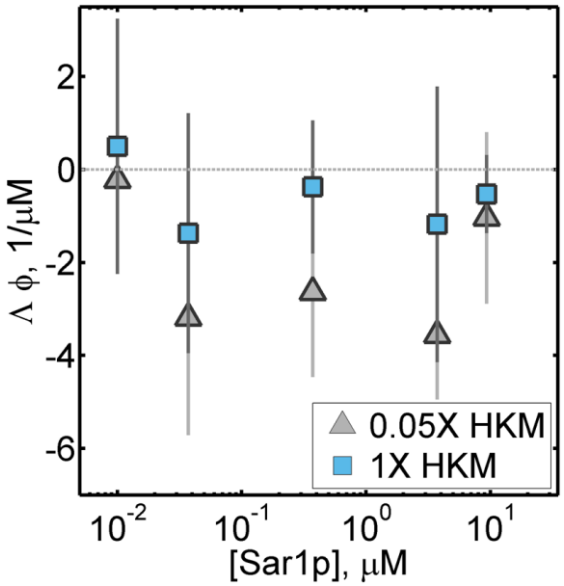

Figure 11. Λϕ, a measure of the coupling between Sar1p and local curvature, as a function of [Sar1p]. Negative values indicate an energetic preference for concave curvature. At [Sar1p] = 0, Λϕ = 0, as expected. For comparison, Δ23-Sar1p in 0.05X HKM shows Λϕ = (-9.9 ± 1.1) x 10^{-20} J/μm. The values and uncertainties are determined from a linear fit of *f*R vs. *R* (Equation 2).

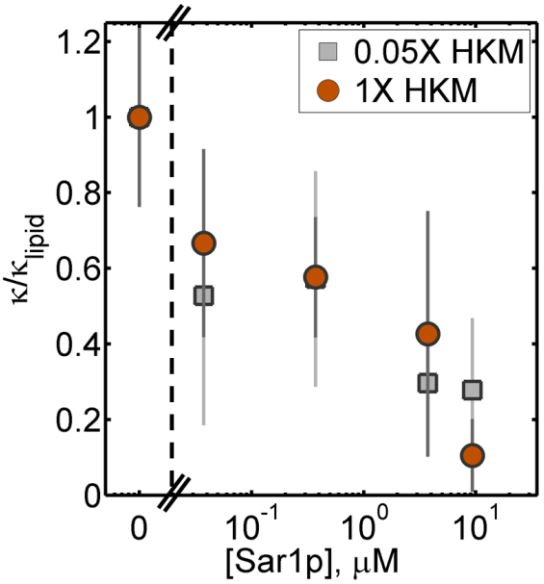

Figure 12. Normalized membrane rigidity, κ, as a function of [Sar1p]. The values and uncertainties are determined from a linear fit of *fR* versus *R* (Equation 2).

Tension measurements

The effective membrane tension, σ_0, shows a decline with [Sar1p], especially at high ionic strength (1X HKM) (Figure 13). As noted earlier, both the true membrane tension and the (indistinguishable) interaction energy of the proteins contribute to σ_0. Tension in lipid bilayer membranes may in general be near zero and moreover, unlike rigidity, it depends on extrinsic factors such as surface area and bounded volume that are unlikely to be constant between samples.[55] For mammalian Sar1s we see little change in tension over [Sar1] and discuss this later in the chapter. The decrease of σ_0 as a function of protein concentration is likely an indication, therefore, of repulsive interactions among Sar1p molecules.

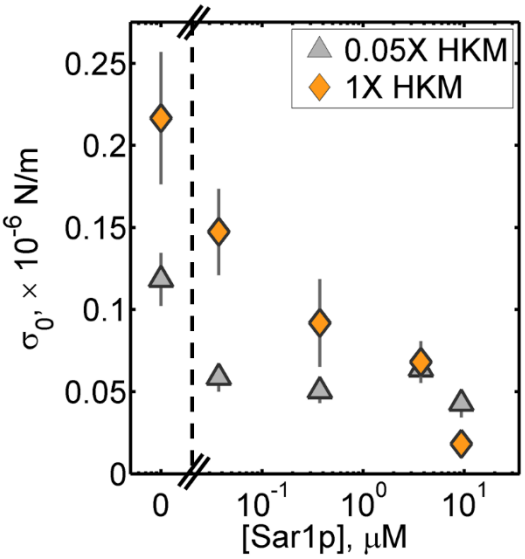

Figure 13. The effective membrane tension, σ_0, as a function of [Sar1p].

Membrane tether homogeneity

The membrane tethers are likely to be single-bilayer shells, because the protein-coated microspheres whose manipulation pulls the tethers are bound only to the outermost surface of the membrane sheet. Although we lack a direct assay for potential

multilamellar structure in the tethers, fluorescence imaging as in Figure 4, allows an assessment of whether there is appreciable polydispersity in structure. The background-subtracted fluorescence intensity integrated over a cross-section of the tether should be proportional to the circumference of the tether and to the number of layers in the cylindrical shell. The intensity normalized by tether radius, therefore, is proportional to the multilamellarity. In practice, differences in fluorescence illumination intensity and photobleaching will contribute to differences in tether intensity. Nonetheless, we found that only 8 % of all the tethers have normalized intensities > 1 SD above the mean intensity. Moreover, on every individual day on which experiments were conducted, during which variation in illumination intensity would be minimal, the ratio of the SD of the integrated intensity to the mean was < 1. We conclude, therefore, that the vast majority of tethers form a homogenous population.

Sar1 binding affinities

As noted above, the mammalian Sar1 proteins differ from Sar1p in their mechanical impact on membranes. To determine whether the different rigidities between Sar1A, B and p simply mirror differences in membrane-bound concentration among the various Sar1s, we determined the binding affinities of the Sar1s. Experiments using reactive fluorophores conjugated to primary amines on the proteins themselves yielded highly variable degrees of labeling. We therefore used a fluorescent non-hydrolyzable nucleotide, BODIPY FL GTP-γ-S, as an indicator of protein abundance. In all experiments, the BODIPY fluorescence intensity (I_{Sar1}) and the fluorescence intensity of Texas Red lipid probes (I_{lipid}) are measured following washing to remove unbound proteins and nucleotide. Normalizing the background-subtracted I_{Sar1} by I_{lipid} (to account

for small variations in illumination intensity) provides the normalized fluorescence intensity plotted in Figure 14. The data show similar two-dimensional protein abundances for all the Sar1 proteins. A fit to a Langmuir isotherm gives a binding constant of K_D = 10.5 ± 3.1 μM, with no significant difference among the Sar1 types. This suggests that differential binding affinities of the protein to the membrane are not the cause of differences in the modulation of the membrane rigidity.

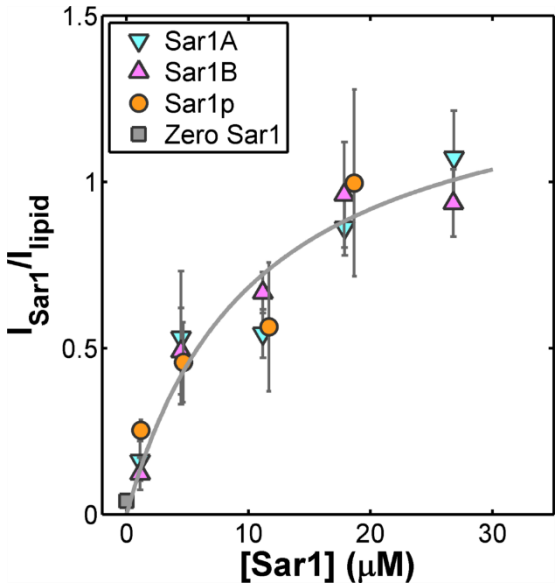

Figure 14. Sar1-membrane binding assay. Normalized intensity of fluorescent nucleotides, providing a measure of membrane-bound protein concentration, as a function of the solution concentration of Sar1. The binding behaviors of all three proteins to the lipid membrane are similar. A Langmuir isotherm fit to all the data (solid curve) gives K_D = 10.5 ± 3.1 μM.

Sar1 and membrane diffusion

Hypothesizing that differences in rigidity may correlate with differences in in-plane mobility, we measured the diffusion coefficients of lipids (D_{lipid}) and membrane-bound Sar1 proteins (D_{Sar1}) by performing fluorescence recovery after photobleaching (FRAP) experiments on fluorescent lipid probes and fluorescent nucleotides.[66,67,69] We

show in Figures 15A and 15B examples of photobleached spots and their recoveries for both the lipid and protein probes. Throughout the full range of concentrations examined, lipids and proteins are all mobile, implying that none of the Sar1 proteins form a rigid structured scaffold. Quantification of the diffusion coefficients reveals differences in the behaviors of the yeast and human Sar1s. As a function of concentration, D_{Sar1} is roughly constant for Sar1p, while it decreases significantly for the human Sar1s (Figure 15C). The low mobility at high concentrations is more pronounced for Sar1A than Sar1B (Figure 15). This trend is also reflected in the lipid diffusion coefficients. At [Sar1] ≈ 20 μM, D_{lipid} with bound Sar1p is 5.1 ± 1.0 $\mu m^2/s$, identical within uncertainties to the value with no protein, 5.6 ± 0.6 $\mu m^2/s$. In contrast, D_{lipid} = 2.7 ± 0.5 $\mu m/s^2$ for Sar1A and 3.0 ± 0.4 $\mu m/s^2$ for Sar1B.

DISCUSSION

Our measurements reveal that Sar1p dramatically lowers the rigidity of lipid bilayer membranes, the first such discovery for a vesicle trafficking protein. This membrane softening does not coincide with the imposition of strong local curvature, and is a profoundly different mode of action than those typically ascribed to intracellular curvature-associated proteins, such as the construction of rigid scaffolds[5-7,70] or the sensing of local geometry.[71,72] Sar1 alters the mechanical properties of the membrane to which it binds. We suggest that this synergistic activity on the part of both membrane and protein facilitates coat formation by the rest of the COPII proteins, especially the rigid, cage forming Sec13/Sec31 heterodimer[8], by locally lowering the energetic cost of membrane deformation, proportional to rigidity.

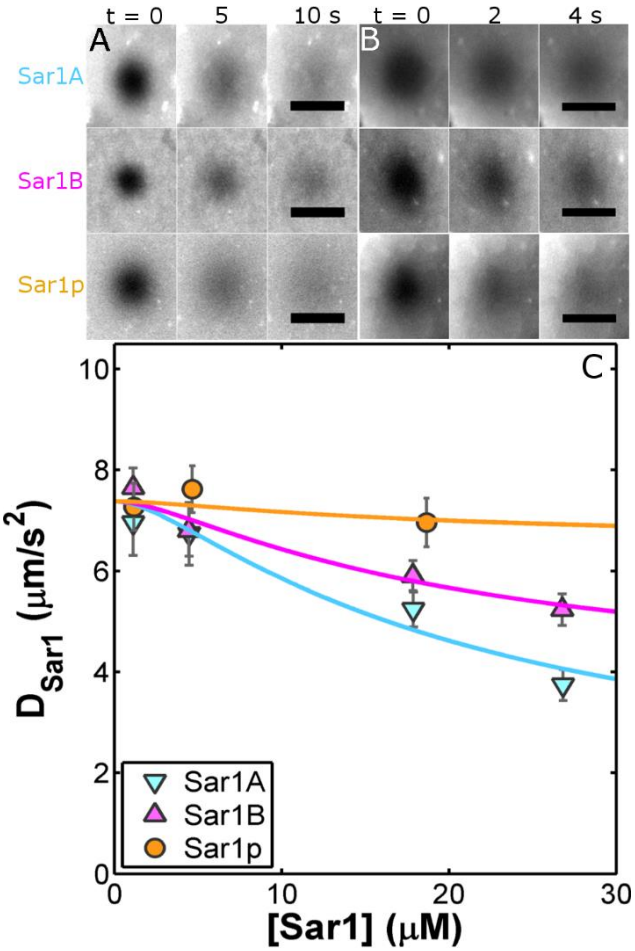

Figure 15. Membrane and Sar1 diffusion assay. (A) Time-lapsed fluorescence images of Texas Red DHPE during FRAP experiments probing membrane mobility. The three rows correspond to membranes incubated with Sar1A, Sar1B, and Sar1p. (B) Time lapse-fluorescence images of BODIPY FL GTP-γ-S during FRAP experiments probing the mobility of membrane-bound protein. (C) Protein diffusion coefficients as a function of incubation concentration for the various Sar1 proteins. Solid lines are fits to the model discussed in the text. Scale bars in (A) and (B) are 25 μm.

We suggest that the lack of significant curvature generation by Sar1, i.e., the small $\Lambda\phi$, is a structural consequence of the positive (convex) Λ expected from the bilayer insertion of the N-terminal helix[29,15] being counteracted by the negative (concave) Λ induced by the rest of the protein (Δ23-Sar1p, Figure 9). It should be kept in mind that our finding of small $\Lambda\phi$ means only that Sar1 does not necessarily couple strongly to curvature; spatial constraints may still enable it to contribute to membrane bending

independent of other COPII coat proteins. Particular geometries (as in the case of liposome-binding[15,16]) or interactions with other proteins or lipids (e.g., that localize it to particular regions of the ER membrane), could spatially enhance asymmetries in leaflet areas and generate curvature via the bilayer couple mechanism noted earlier.

The rigidity, mobility, and binding affinity measurements suggest that the human Sar1 proteins, unlike yeast Sar1, may interact with one another at the membrane, forming assemblies that are stiffer and less mobile than membranes solely bound by protein monomers. While an infinite number of models could be concocted to mimic these observations, our ignorance of the structural mechanisms of potential inter-protein interactions motivates a minimalist approach of constructing the simplest possible non-trivial model, asking whether the functional form of the rigidity and mobility it predicts are mirrored by the data, and allowing only a small number of free parameters. Our simple model assumes that all Sar1 proteins lower membrane rigidity by an amount proportional to their two-dimensional concentration that Sar1A and Sar1B proteins have a weak affinity for dimerization, and that rigidity and mobility induced by Sar1A and Sar1B are proportional to the dimer concentration. Of course, higher order dependences of rigidity and mobility on concentration, as well as higher order oligomerization, are possible; invoking them would introduce additional parameters.

We decompose the membrane bending rigidity (κ) into the sum of the rigidities induced by individual proteins (κ_s) and by dimers (κ_{dimer}):

$$\kappa = \kappa_s + \kappa_{dimer}. \qquad \text{(Eq.5)}$$

Neglecting dimerization, we propose that Sar1 proteins monotonically lower κ_s, the simplest form for which is a linear decrease in rigidity as a function of membrane-bound protein concentration:

$$\kappa_s = \kappa_{lipid}(1 - \alpha^{-1}c). \quad \text{(Eq.6)}$$

Where κ_{lipid} is the rigidity in the absence of protein, c is the two-dimensional concentration of the protein at the membrane normalized by the maximal protein density, and α is the critical concentration at which the membrane reaches zero rigidity. By construction, $\alpha \leq 1$, the empirically determined value of this parameter is discussed below. The rigidity κ_s is constrained to be non-negative.

The two-dimensional concentration, c, as a function of the solution concentration of protein, [Sar1], is provided by the binding data shown in Figure 14, which can be fit to a Langmuir isotherm:

$$c = \frac{[Sar1]}{K_D + [Sar1]}. \quad \text{(Eq.7)}$$

The equilibrium between membrane-bound monomers (p) and dimers (p-p), written as $p + p \leftrightarrow p\text{-}p$, implies that $c_d = K_2 c_m^2$, where c_d and c_m are the two-dimensional concentrations of dimers and monomers, respectively, and K_2 is the binding constant. For weak binding, i.e. to lowest order in $K_2 c$, $c_d \approx K_2 c^2$, providing a simple relationship between dimer density and overall membrane-bound concentration.

We propose that dimers increase rigidity, since they correspond to fixed spatial arrangements of membrane-bound proteins, and that the dimer-induced rigidity is directly proportional to c_d, from which

$$\kappa_{dimer} = \kappa_p c^2, \quad \text{(Eq.8)}$$

where the parameter κ_p characterizes the dimer stiffness and binding affinity. (In other words, $\kappa_{dimer} = Bc_d$ for some stiffness parameter B, which can be written $\kappa_{dimer} = BK_2c^2$. Since K_2 and B are not separately measurable, we subsume them into a single parameter, κ_p.).

Equations 5-8 characterize our model. The parameters α, K_D, and κ_p in principle could be different for all the proteins, but in practice are highly constrained by data. As noted above, the membrane-binding affinity is $K_D = 10.5 \pm 3.1$ μM for all the proteins. The rigidity in the absence of protein, κ_{lipid}, is directly measured. (Alternatively, κ_{lipid} can be treated as a fit parameter; this is discussed in Appendix A). We assume that Sar1p does not dimerize, and so its $\kappa_p = 0$, allowing its rigidity data (Figure 7A) to be fit with only one free parameter, α, yielding $\alpha = 0.56 \pm 0.02$. Using this same α for the human Sar1 proteins (i.e. treating the membrane softening, not related to dimerization, as being the same for all Sar1s), we can fit the Sar1A and Sar1B rigidity data with only one free parameter, κ_p, for each protein species. We find good agreement between the data and the form of κ predicted by the model (Figure 8A, solid curves), and find for Sar1A, $\kappa_{p,Sar1A}/\kappa_{lipid} = 2.3 \pm 0.44$, and for Sar1B, $\kappa_{p,Sar1B}/\kappa_{lipid} = 1.4 \pm 0.38$, quantifying the greater rigidity of Sar1A relative to Sar1B observed in tether-pulling experiments.

We can similarly ask whether the protein diffusion coefficient (D_p) decreases proportionally with dimer concentration:

$$D_p = D_0 (1 - dc^2), \qquad \text{(Eq.9)}$$

where D_0 is the diffusion coefficient at [Sar1] $\rightarrow$ 0 and d is a dimensionless parameter. Fitting the data shown in Figure 14C yields $D_0 = 7.4 \pm 0.2$ μm/s^2 for all the proteins. For Sar1A, we find $d_{Sar1A} = 0.87 \pm 0.13$ and for Sar1B $d_{Sar1B} = 0.54 \pm 0.08$. The Sar1p data show $d_{Sar1p} = 0.12 \pm 0.11$, consistent with negligible dimerization.

Notably, the ratio of the mobility reductions for the human proteins $d_{Sar1A}/d_{Sar1B} = 1.6 \pm 0.3$, identical within uncertainties to the ratio of the relative rigidity parameters: $\kappa_{p,Sar1A}/\kappa_{p,Sar1B} = 1.6 \pm 0.6$. The similarity of these ratios for two independently measured and physically distinct physical properties further supports the proposed model, in which the existence of dimers of the human Sar1 proteins is the shared determinant of increased stiffening and lower mobility. Unpublished results from Professor Scott Stagg's group at Florida State University has revealed a possible dimer conformation on membrane tubules in cryo-EM studies leading to support of such a model. We stress, however, that the validity of the model is separate from the main experimental conclusions of this section, that the human Sar1 proteins non-monotonically alter membrane rigidity as a function of concentration. We believe the model provides a useful framework for envisioning the possible molecular mechanisms underlying our observations, and hope that this may spur studies of weak interactions among membrane-associated proteins that may be feasible using recently developed resonance energy transfer or correlation spectroscopy techniques.[73]

BRIDGE

As our measurements reveal Sar1p lowers membrane rigidity monotonically as a function of concentration while Sar1A and Sar1B lead to a lesser reduction and an increase in the membrane rigidity at higher concentrations. As noted earlier, our

measurements of Sar1 provide the first example of trafficking proteins that lower membrane rigidity. Studies of this sort could be improved by higher-throughput experimental methods, and by comparison of different rigidity-measuring techniques. In the next chapter, we do exactly this with thermal vesicle fluctuations and selective plane illumination microscopy.

CHAPTER III

ROBUST MEASUREMENT OF MEMBRANE BENDING MODULI USING LIGHT SHEET FLUORESCENCE IMAGING OF VESICLE FLUCTUATIONS

Reproduced with permission by *Andrew F. Loftus, Sigrid Noreng, Vivian L. Hsieh, and Raghuveer Parthasarathy* 2013. *Langmuir* 29, 14588-14594, Copyright 2013 Langmuir.

Despite their importance, measurements of membrane rigidity are not common, especially for systems that include membrane-associated proteins as well as lipids. We believe this to be due in large part to a lack, compared to other areas of biophysical research, of development and refinement of measurement techniques, and lack of cross-validation of disparate techniques. To address this, we show that the combination of light sheet fluorescence microscopy and vesicle fluctuation analysis enables robust measurements of the bending modulus of lipid and protein membranes, and that these measurements are in close agreement with values from tether-pulling assays.

Techniques for measuring membrane rigidity generally fall into two categories: (1) tether pulling methods and (2) methods based on shape deformations of giant unilamellar vesicles (GUVs). In the first case, a tubule of membrane is pulled from the bulk by application of a local force, using e.g. a magnetically or optically trapped microparticle or a micropipette.[74] By measuring the tether-associated force and geometry, one can determine the rigidity and tension of the system as described in Chapter II and Appendix A.[38,50] While insightful and relatively easy to analyze, tether pulling

experiments are low-throughput, requiring significant time to obtain statistically meaningful data.

Experiments involving vesicle deformations usually make use of imaging thermally driven membrane fluctuations.[40-41,43,47,75] The analysis of thermal fluctuation spectra to obtain rigidity and tension are described in Refs. [42,76]; more recently Méléard et al. have extended this approach to incorporate the statistical distribution of mode amplitudes, which significantly improves the robustness of the analysis.[46] However, several factors complicate fluctuation-based assays, however. Studies to date have considered giant unilamellar vesicles (GUVs) settled at the bottom of a chamber in order to be close to an imaging objective lens, leading to gravitational shape distortions that complicate the application of quasi-spherical analysis models.[43,75] High-speed imaging of the vesicle membrane is generally provided by phase-contrast microscopy[46,42,75], making quantitative estimation of the edge localization precision difficult.

Vesicle-based experiments using electric-field induced deformations[45,77] involve fitting the change in surface area versus the stress caused by the field to a model of tension-induced suppression of fluctuations. Analysis of these deformations are subject to several assumptions about the form of the electric field, chamber geometry, and vesicle location.[77]

For all of these reasons, values in the literature of the bending modulus of even simple single-component lipid membranes show a large spread. For 1-palmitoyl-2-oleoyl-*sn*-glycero-3-phosphocholine (POPC), for example, discussed below, reported κ values range from 2.5×10^{-20} J[45] to 15.8×10^{-20} J.[43] Moreover, to the best of our knowledge,

there are no comparisons of tether-based and vesicle-deformation-based measurements of the same membrane system, either with or without proteins, leaving unanswered the key question of whether the high degree of variation noted above stems from differences in sample preparation or from systematic differences inherent in the various methods.

We aim, therefore, to demonstrate and validate an improved method for measurements of membrane rigidity: the use of selective plane illumination microscopy (SPIM) for vesicle fluctuation imaging. In SPIM, also known as light sheet fluorescence microscopy, a laser is formed into a thin sheet that excites fluorophores in one plane of the sample, the emission from which is imaged onto a camera using a perpendicular objective lens (Figure 16).[78-81] In recent studies, the fast three-dimensional imaging and inherent low photon flux that SPIM makes possible have been applied to investigations of animal and plant development.[80,79,82] SPIM has not, however, been previously applied to *in vitro* membrane systems. We realized that SPIM's attributes for multicellular imaging are also ideal for visualizing vesicle fluctuations: Its optical sectioning enables high speed imaging of the equatorial plane of GUVs, its use of fluorescence provides ring-like images of the vesicle edge (Figure 16) whose localization precision can be assessed with simple models, and its applicability to thick samples allows the imaging of freely suspended GUVs far from a chamber wall.

We show that SPIM imaging of GUV membrane fluctuations provides data that are well-fit by models of vesicle fluctuation spectra.[46] We measure values for the bending modulus of POPC membranes and membranes bound by various concentrations of Sar1p, shown previously to lower membrane rigidity (see Chapter II for details). For each of these systems, SPIM-imaged fluctuation-derived values are in close agreement with

values from tether pulling assays (within at most 20 %). We also show that the human Sar1A protein, shown in Chapter II to increase membrane rigidity and potentially self-associate, gives fluctuation spectra that are not well fit by a model of homogenous vesicles.

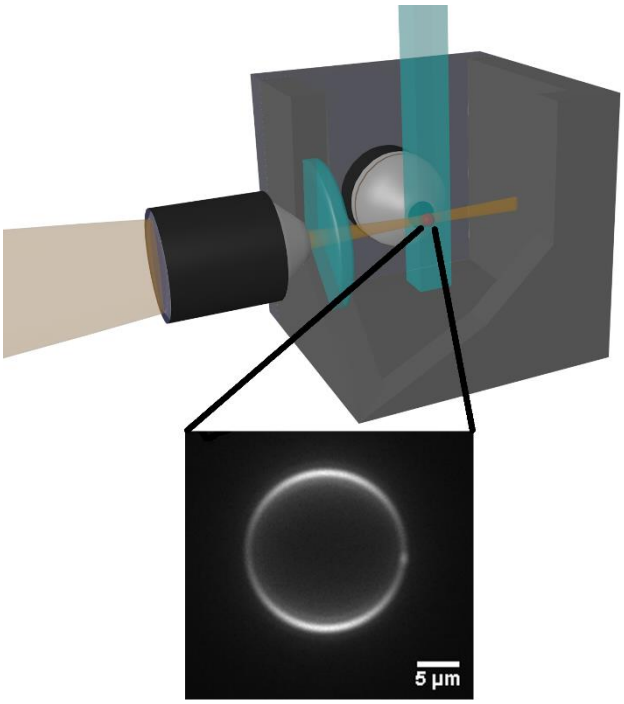

Figure 16. Schematic application of SPIM to image GUVs. A thin sheet of excitation light coincident with the focal plane of an imaging objective allows high-speed optical sectioning of a suspension of lipid vesicles. Inset: image of a POPC vesicle with 2 mol % Texas Red DHPE fluorescent lipids.

EXPERIMENTAL METHODS

Lipid composition

Briefly, two lipid membrane mixtures were composed for GUV fluctuation and tether pulling studies: (1) 98 mol % POPC, 2 mol % Texas Red DHPE and 1.0 mol % biotinyl-cap-PE. (2) The Major Mix as reported in Chapter II and Appendix A. For GUV fluctuation studies Major Mix composition was composed of 2 mol % Texas Red DHPE with the other lipids proportionally scaled.

Protein purification and nucleotide binding

Sar1 was expressed and purified using protocols similar to those in Barlowe *et al*.[83] Chapter II describes in detail the protocol for purification and nucleotide binding.

Tether pulling assay

Tether pulling using an optical trap was performed as previously described in Chapter II and Appendix A. Particle position was tracked with home-built MATLAB programming as previously described in Chapter II and Ref [84].

Calculation of bending rigidity from membrane tethers

The retraction of pulled membrane tethers allows determination of the membrane rigidity. As described in Chapter II, the bending rigidity in the absence of spontaneous curvature (κ_0) was calculated from the tether retraction force (f) and tether radius (R) using equation 2.

Vesicle electroformation

GUVs were created by electroformation as described by Herold et al.[85] Briefly, lipids were deposited on air annealed indium-tin oxide (ITO) glass slides, R_s = 15-25 Ω (Delta Technologies), and dried under vacuum for 10 min. A chamber was assembled from two ITO-glass slides separated by a 1.5 mm gasket of silicon rubber and sealed with binding clips. The electroformation chamber was then gently filled with 0.1 M sucrose solution. After this a sinusoidal AC electric field of 1.2 V_{rms} at 10 Hz was applied to the chamber for 2 h. The GUV suspension was gently pulled out of the chamber with a syringe.

Selective plane illumination microscopy

GUV suspension (10 μL), with or without protein, was placed in a square micro fluorometer cell (Starna Cells) containing 200 uL of 0.25 M sucrose solution. Selective plane illumination microscopy of vesicles was performed using a home-built setup similar to that of Ref. [80] and described in detail in Ref. [82]. Key components are listed in Appendix C (Table S1). Briefly, a 594 nm diode laser with a power of 50 mW (Lasermate) provided excitation light for the Texas Red fluorophore labeling lipids. The light is passed through an acousto-optic tunable filter and is then incident to a rapidly scanning (2 kHz) galvanometer mirror. A telecentric scan lens transforms the angular scan into a translating scan that passes through a tube lens and an objective lens producing a thin sheet of light in the sample holder. The beam thickness was measured to be 3.0 μm over a lateral extent of ≈ 100 μm. Images were captured through a 40x 1.0 NA Plan-apo objective lens (Zeiss) perpendicular to the excitation plane and recorded with a 5.5 Mpixel sCMOS camera (pco.edge, Cooke Corp., pixel size 6.5 μm) at an exposure time of 500 μs with a frame rate range of 60-200 fps.

The camera exposure time is much smaller than the timescale of the fluctuations of the examined vesicle modes, which are calculated to be over 10 ms up to m = 35 for vesicles of the measured rigidity and radius values[46], and hence any corrections to the analysis due to finite exposure times will be very small compared to the observed statistical variation between vesicles.

Edge determination

The location of the vesicle edge was calculated for each two-dimensional image using home-built software written in MATLAB. Starting from a rough, user-input

estimation of the center of the vesicle in the initial frame, each image is divided into several (50-300) angular wedges. In each wedge, the vesicle edge is determined by locating the pixels of maximal intensity gradient in the radial direction, and then further refined by finding the peak of a local parabolic fit to the intensity gradient.

To determine the precision of this edge determination method, we applied it to simulated images of fluorescent rings with various radii and signal to noise ratios (SNRs), mimicking the form of the optically sectioned vesicle images. The difference between the true and estimated edge locations at SNR values corresponding to the experimental SNR gives a measure of the experimental localization precision. The simulated images were created in a similar manner to images of rings described in Ref. [84]; in brief, a high-resolution image of a thin annulus was convolved with the imaging point-spread function, pixelated, and subjected to Poisson-distributed noise. For simulated ring images, we used the theoretical point spread function for the imaging wavelength and numerical aperture, which has a width of 250 nm. We also experimentally measured the PSF by imaging fluorescent beads immobilized in agar gel. Fitting the intensity profiles of beads to a 2D Gaussian yielded point spread function widths within 10 % of the theoretical value.

The standard deviation of the calculated radial positions of the simulated vesicle edges, which would be zero for perfect edge detection, provides a measure of the image analysis precision. The SNR of experimental images was estimated as the ratio of the peak intensity at the vesicle edge to the standard deviation of the background intensity, and the precision of the edge determination was assessed as the precision of the localization of the simulated images at that SNR.

Calculation of bending rigidity from vesicle fluctuations

The vesicle edge ρ(η, *t*), where ρ and η are the radial and angular coordinates, respectively, from an image obtained at time *t* is determined as described above. These edge profiles are analyzed to reveal the underlying membrane rigidity and tension using the procedure described in Refs. [42,46]. In brief, the angular autocorrelation function:

$$\xi(\gamma, t) = \frac{1}{2\pi R^2}\int_{\varphi=0}^{2\pi}[\rho(\eta+\gamma, t) - \rho(t)] \times [\rho(\eta + t) - \rho(t)]\, d\eta, \qquad \text{(Eq.10)}$$

where ρ(t) is the mean of ρ, is cosine decomposed

$$\xi(\gamma, t) = \sum_{0<m}^{n_{max}} \chi_m(t)\cos(m\gamma), \qquad \text{(Eq.11)}$$

to give the mode amplitudes χ_m. As described in Ref. [46], each mode amplitude should follow an exponential (Boltzmann) probability distribution:

$$\Gamma_m(\chi_m) \propto exp\left[-L_m \frac{\chi_m}{2}\right], \qquad \text{(Eq.12)}$$

where $\Gamma_m(\chi_m)$ is probability of observing χ_m, and the L_m values (denoted R_m in Ref. [46]) are determined from exponential fits to the measured χ_m distribution over the range for which Γ is at least one-tenth of its maximal value to exclude rare outliers.[46]

The L_m values are then fit via least-squares minimization to the expected theoretical form for the mode-dependence of quasi-spherical vesicle fluctuations, for which the rigidity and tension are the two unknown parameters:

$$L_m(\kappa/k_bT, \bar{\sigma}) = \frac{\kappa}{k_bT} \times \frac{1}{\sum_{n\geq m}^{n_{max}}[Q_n^m(0)]^2/\lambda_n(\bar{\sigma})}, \qquad \text{(Eq.13)}$$

where κ is the membrane bending modulus, $\bar{\sigma}$ the reduced membrane tension $\bar{\sigma} = \sigma R^2/\kappa$, k_b being Boltzmann's constant, $\lambda_n(\bar{\sigma})$= (n+2)(n-1)[$\bar{\sigma}$+n(n+1)] , and Q_n^m is given by:

$$Q_n^m(cos\theta) = (-1)^m \sqrt{\frac{2n+1}{4\pi}\frac{(n-m)!}{(n+m)!}} P_n^m(cos\theta), \quad \text{(Eq.14)}$$

where $P_n^m(cos\theta)$ is the associated Legendre function. For individual vesicles, the fit uncertainty for the rigidity is on average 25 % of the measured value, ranging from 10 % to 55 %. The stated rigidity values are the sample means across distinct vesicles, with the uncertainty given as the standard error of the mean.

Precision of bending rigidity determination

To determine the impact of edge localization precision described above on the determination of κ, we numerically propagated the position uncertainty through the functions that relate position to κ (Eqns. 10-14). We performed multiple tests in which we replaced the edge positions of vesicles with a random number drawn from a Gaussian distribution centered on the measured position and with a width equal to the localization precision at experimental SNR, and then analyzed contour profiles and fluctuation spectra to determine the resulting values of κ. The standard deviation of the resulting κ values provides a measure of the uncertainty due to localization precision.

RESULTS

SPIM imaging of homogeneous giant unilamellar vesicles shows fluctuations whose spectra are well fit by theoretical models. Figure 17A shows a series of images from one vesicle, together with the image-derived edge positions (Figure 17B). As expected, the probability distribution of the mode amplitudes $\Gamma_m(\chi_m)$ is exponential (Equation 12, Figure 2C), yielding a logarithmic slope L_m that decays with mode wavelength $\lambda_m = 2\pi R/m$, where R is the vesicle radius (Figure 17D). The form of $L_m(\lambda_m)$ is well fit by the theoretical expectation for thermal fluctuations of homogeneous quasi-spherical vesicles [46], illustrated for one vesicle in Figure 17D. Notably, the statistical

approach to fluctuation amplitudes introduced in Ref. [46] (see Experimental Methods) is robust even in the presence of minor imperfections in vesicle morphology, as can be seen in Figure 17. Less imperfect vesicles were also routinely examined, as represented in Appendix C.

SPIM-based fluctuation analysis of lipid-only vesicles composed of 98% POPC (see Experimental Methods) yields spectra that are well fit by expected theoretical forms (Appendix C, Figure S2), yielding an average rigidity value over N = 32 vesicles of $\kappa = 12.1 \pm 1.9 \times 10^{-20}$ J. Moreover, we are able to measure bilayer rigidity using a completely independent technique, the pulling of membrane tethers from lipid multilayers.[34-35,38,50] These measurements of POPC lipids yield a value of $\kappa = 10.6 \pm 1.7 \times 10^{-20}$ J. Notably, the two techniques give similar values, within uncertainties of each other. We find that the average vesicle tension is 1.45×10^{-7} N/m with a standard deviation of 3.30×10^{-7} N/m, in the range generally observed for electroformed vesicles.[75]

As detailed in Experimental Methods, fluorescence imaging of vesicle edges allows quantification of the precision of radial position determination via examination of simulated vesicle images. The experimental signal-to-noise ratios for the vesicle edges are in the range 5-20; regions of brighter and dimmer intensity are due to the geometry-dependent angle between the excitation dipole of the Texas-Red fluorophore, which orients in the plane of the lipid bilayer[86], and the linearly polarized excitation laser light. These SNRs give an average precision of ≈ 10 nm. As described in Experimental Methods, this results in a localization-based uncertainty in κ of $\approx 0.1 \times 10^{-20}$ J, which is small compared to the statistical variation in rigidity between vesicles (Figure 18).

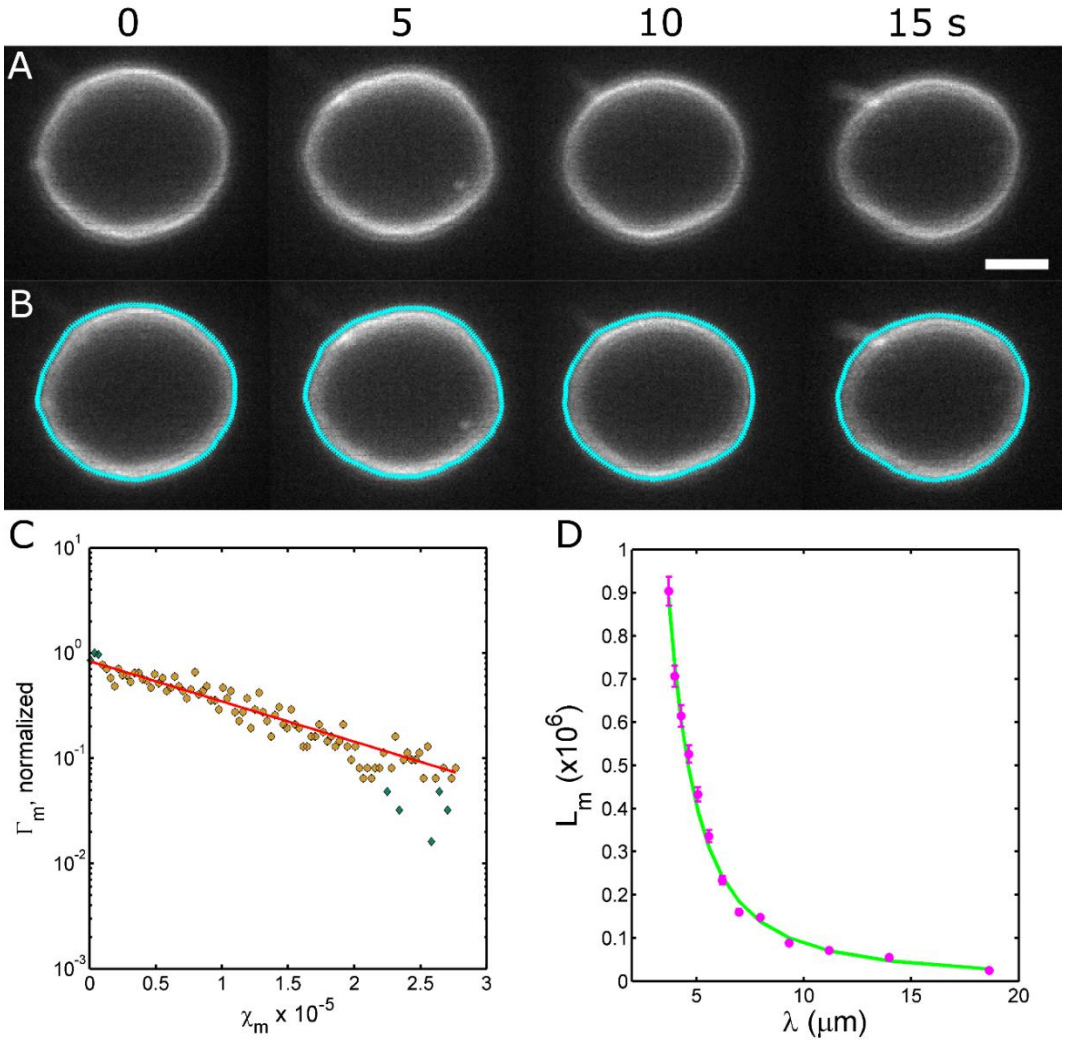

Figure 17. Fluctuation analysis. (A) A series of fluorescence images (Texas Red DHPE) of a lipid vesicle incubated with 3.7 μM Sar1p, with (B) superimposed edges determined from radial gradient maxima. (C) Histogram of autocorrelation amplitudes χ_m for mode m = 4 (λ = 14.0 μm) from 2000 images. The solid line is an exponential fit to the points shown in orange and blue points are not fit because their occurrence is < 10 % of the peak; the uncertainty in the fitted slope is 4 %. (D) L_m values (circles) as a function of mode wavelength (λ = 2πR/m) and the best-fit theoretical curve (green line), which gives a bending modulus κ = (3.1 ± 0.5) x 10^{-20} J and tension σ = 3.0 x 10^{-8} N/m for this vesicle.

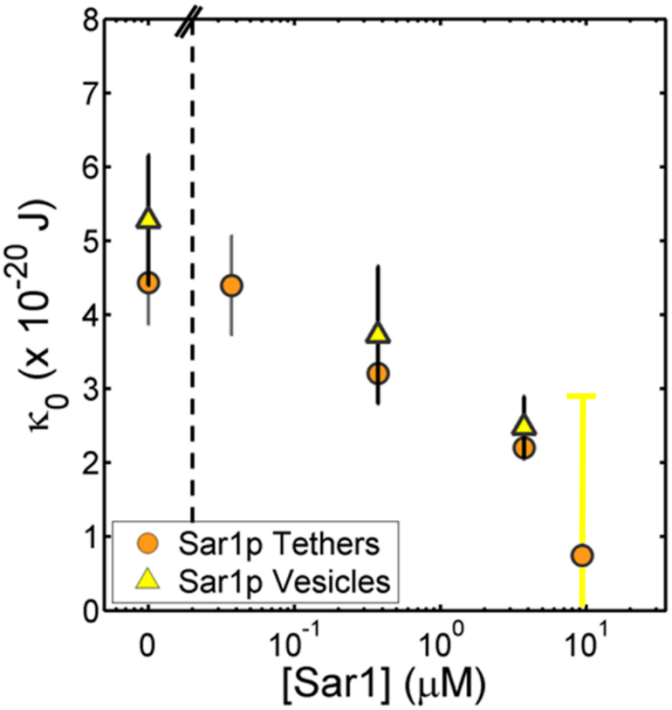

Figure 18. Membrane rigidity comparison. Membrane rigidity determined from tether pulling studies (orange circles, reported in Chapter II), and vesicle fluctuations (yellow triangles) as a function of Sar1p concentration. At a [Sar1p] ≈ 10 μM, spontaneous tubulation and budding of the majority of vesicles prevents fluctuation analysis; the plotted rigidity (yellow upper bound bar) is derived from the minority of non-tubulating vesicles and so is likely an upper bound on rigidity.

We next present rigidity measurements based on light sheet fluctuation imaging of a system for which earlier tether-based measurements demonstrated protein-induced modulation of membrane rigidity, namely the intracellular trafficking protein Sar1p binding to Major Mix lipids that mimic the composition of the endoplasmic reticulum.[24] As shown in Figure 17, GUVs incubated with Sar1p show fluctuation behavior that is well fit by conventional theory. We provide videos of representative vesicles incubated with 0 and 3.7 μM Sar1p as Videos S2 and S3 in Appendix C and the supplemental files included with this dissertation, respectively. In Figure 18 we plot the previously obtained tether-derived measurements together with new vesicle-based values. From 0-4 μM Sar1p, rigidity values from the two techniques are very similar. At 9 μM Sar1p (yellow

upper bound line, Figure 18), many vesicles had disintegrated, forming multiple tubules or budding daughter vesicles, and so could not be analyzed in the framework of quasi-spherical vesicle fluctuations.[46] The data point shown at 9 μM Sar1p is from a small number (N=6) of intact vesicles, which were a minority of those found in solution, and so should be considered an upper bound for the rigidity.

In Chapter II we showed that Sar1A and Sar1B; lower membrane rigidity at low concentrations but raise it at concentrations above ≈ 10 μM. However, tether-based rigidity measurements were difficult at higher concentrations because tethers were often impossible to pull, presumably because the force required exceeded the available optical trapping strength. Imaging vesicle fluctuations allowed estimation of membrane rigidity in the presence of high concentrations of the mammalian Sar1 proteins. For example, rigidity at 36 μM Sar1A was on average ≈ 30 x 10^{-20} J, over six times that of the lipid bilayer in the absence of protein, and approximately two times the maximum value that could be probed by tether-based investigations.

An additional attribute of fluctuation analysis is that the form of the fluctuation spectra provides information about possible scale-dependent vesicle mechanics. For Sar1A, the L_m values are not well fit by the theoretical expression for homogenous, quasi-spherical vesicles (Figure 19A; compare with Figure 17D for Sar1p), and show non-random deviation from the expected form (Figure 19B). Notably, the individual χ_m remain exponentially distributed (Appendix C, Figure S3), as would be expected for thermally driven modes.

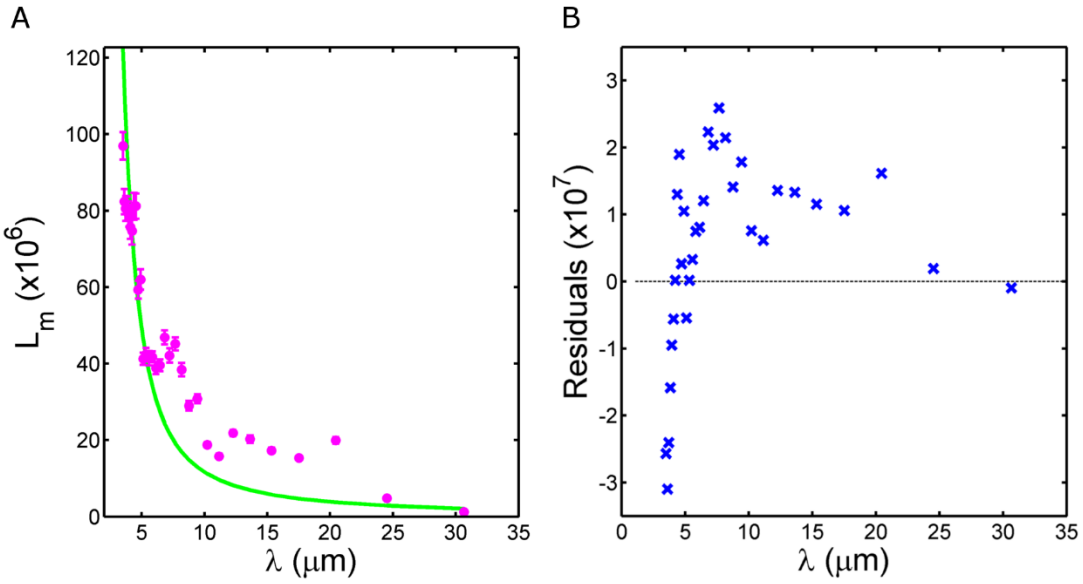

Figure 19. Sar1A fluctuation analysis. (A) L_m as a function of mode wavelength for a vesicle incubated with 36 μM Sar1A. The data poorly fit the expected form for fluctuations of homogeneous quasi-spherical vesicles (solid curve, rigidity 26 x 10^{-20} J). (B) Residuals of the fit in (A). The data show a nonrandom form implying a systematic deviation from the expected theory.

SUMMARY

We have demonstrated the utility of using light sheet fluorescence microscopy and thermal fluctuation analysis for measuring membrane bending moduli. SPIM provides several advantages over conventional fluctuation imaging due to its use of fluorescent probes, enabling quantifiably precise edge determination, and its applicability to freely suspended vesicles, avoiding gravitational distortions at chamber walls. We find a bending modulus for POPC membranes of $\kappa = 12.1 \pm 1.9 \times 10^{-20}$ J, indistinguishable within uncertainty of the value determined by the independent technique of membrane tether pulling. The concordance is especially notable given the large spread of rigidity values for POPC noted in the literature, ranging from 2.5 to 15.8 x 10^{-20} J (Table 2, Figure S5). For protein-bound membranes, we similarly find a close agreement between fluctuation-derived and tether-derived bending modulus values (Figure 18). Notably, our

results provide the first reported comparisons of rigidity measurements using vesicle-based and non-vesicle-based techniques by the same group applied to the same systems, and the similarity of the outcomes suggests membrane rigidity may be more robustly measurable than the existing literature would imply.

Table 2. κ values for POPC membranes measured by vesicle and tether based methods

Reference Number (Year)	Vesicle Deformations	Vesicle Fluctuation Analysis	Tether Pulling
This Work	-	12.1 ± 1.9	10.6 ± 1.7
44 (2012)	-	-	6.70 ± 2.00
48 (2012)	3.27 ± 0.19	-	-
46 (2011)	-	12.9 ± 0.04	-
41 (2010)	-	15.80 ± 0.33	-
40 (2008)	-	9.87 ± 0.30	-
43 (2004)	-	13.00 ± 0.40	-
47 (1995)	5.89 ± 1.18	3.96 ± 0.87	-
45 (1991)	2.47 ± 0.49	-	-

Our vesicle fluctuation imaging also highlights two sorts of systems for which this approach can fail. For high concentrations of the membrane-softening protein Sar1p, disintegration of vesicles leaves only a small and non-representative fraction left for analysis. For high concentrations of the rigidity-enhancing Sar1A, the observed fluctuation spectrum is not well fit by theory (Figure 19A). Given prior observations of low diffusion rates at high concentrations that led to a model of weak inter-protein binding by Sar1A, this may suggest a picture of a protein mesh such that below the characteristic mesh size, the effective rigidity is similar to that of the lipid membrane, and above, it takes a larger value characteristic of the protein network. Investigating this model will require more experimental work, as well as a better theoretical understanding of the fluctuation spectra that should arise for inhomogeneous quasi-spherical vesicles.

For both simple and complex membrane systems, however, we believe that light-sheet based fluctuation analysis provides a powerful route to characterizing membrane physical properties.

Still more broadly, we introduce the application of light sheet fluorescence microscopy to studies of membrane biophysics. This imaging technique has attracted a great deal of attention in recent years due to the insights it allows into embryonic development.[78-82] Its utility for non-living systems has been remarkably unrealized, however, and we look forward to its further applications to dynamic interfaces and soft materials.

BRIDGE

Having developed robust methods for measuring membrane rigidity using our two independent measurements allows for the confidence to determine the rigidity of lipid only and lipid-protein systems. We continue to examine the role of Sar1's amphipathic alpha helix in reducing the membrane rigidity, and attempt to form scaffolds with amphipathic helices to produce artificial vesicles. The proceeding chapter will discuss this and provide a future perspective as well.

CHAPTER IV

HELICAL STUDIES FOR MEMBRANE RIGIDITY REDUCTION

Reproduced with permission from Settles, I., Loftus A.F., McKeown, A. N. and Parthasarathy R. *Biophysical Journal* 99: 1539-1545. Copyright 2010, Biophysical Journal.

Unpublished work with contributions from Andrew F. Loftus, Vivian L. Hsieh, Alex MacLeod, David Rabuka and Raghuveer Parthasarathy

To further our understanding of Sar1's ability to modulate the bending modulus of the ER membrane, we examine the role of its amphipathic alpha helix. In Chapter II, I described how deletion of Sar1p's helix (Δ-23 Sar1p) shows no deformations[15] and gives rigidity values similar to the Major Mix only system. We believe the helix is playing a key role in reducing the membrane rigidity by the insertion and subsequent alteration of the membrane structure. We performed measurements to understand the extent the helix is capable of reducing rigidity, by utilizing a synthetic mimic of Sar1p's N-terminal helix. Again, using the tether-pulling assay described in Chapter II.

In addition, we attempted to cross-link helices to build towards more sophisticated mimics of vesicle formation. We believe in order for vesiculation to occur effectively, scaffolds are necessary to organize and localize the concentration of helices to produce deformations and vesicles from the membrane. By creating conjugated scaffolds of the helical peptides, we would be achieving spatial localization seen in trafficking systems.

To accomplish this a bioconjugation technique capable of chemically linking reactive peptides to one another or to a molecule, is a necessity for a multi-helical scaffold. The approach we are using is the aldehyde tagging scheme published by Professor Bertozzi's group.[49] By utilizing aldehyde modified proteins or peptides in the form of formylglycine, the peptide or protein can be chemically conjugated to specific moieties through a hydrazine or hydrazide through the Wolff-Kischner mechanism.[87,88] This provides the capability to link multiple helices to a central molecule with reactive groups to make such a scaffold necessary for our studies. Although we have been unsuccessful so far, attempts to create a peptide scaffold continue to be in progress. I finally consider a perspective to this work and future endeavors that can be undertaken to allow this project to continue forward.

MATERIALS AND METHODS

The fluorescein-conjugated peptide corresponding to the N-terminal alpha-helical domain of Sar1p (FITC-SH) was purchased from Biomatik (sequence from N to C termini: MAGWDIFGWFRDVLASLGLWNKH, with N-terminal FITC). The addition of 5% dimethylsulfoxide (DMSO) to 0.05X HKM was required for peptide solubility and used as is. The 5Fam (5–Carboxyfluorescein) formylglycine modified peptide corresponding to the alpha helical domain of Sar1p (5Fam-SAH) was purchased from New England Peptide (sequence from N to C termini: 5Fam-(dPEG4)-MAGWDIFGWFRDVLASLGLWNKHGG(FGly)-amide). 8-arm-PEG-hydrazine (PEG; 20 kDa) was purchased from Creative PEGWorks. Lipid composition is Major Mix composition as described in Chapter II with 0.5 mol % Texas-Red DHPE and and 1.0 mol % biotinyl-cap-PE for tether pulling experiments.[14]

Aldehyde tagging and experimental setup

We followed a modified aldehyde tagging protocol from Rabuka et. al.[89] We first solubilized 5Fam-SAH in a solution of 5 % Tween-20® (Sigma) and 5 % Dimethylformamide (Sigma) in 1X HKM, the solution was then measured with an ultraviolet-visible spectrometer (8453 Agilent UV-Vis) at 495 nm to determine concentration of peptide in solution. 8-arm PEG hydrazine was weighed out and solubilized in 1X HKM. 8-arm PEG hydrazine solution was added to the 5Fam-SAH in a mole ratio of 1:20 (PEG:5Fam-SAH) and the reaction was lowered to a pH = 6.0 with a solution of 3 M potassium acetate (pH = 4). For the reaction to proceed it is necessary for the solution to be acidic within a pH range = 4.5 - 6.5. The reaction mixture was then covered with foil to protect from photodamage from occurring and left at room temperature overnight. The reaction can also be performed at 37 ^{o}C for as little as 4 h., but led to degradation and precipitation of the peptide. With the completion of the reaction, the sample was then brought back to pH = 7.0 with potassium hydroxide to quench the reaction. The mixture was run through a DetergentOUT™ Tween® column (G-biosciences) to remove any detergent in the solution and a NP-25 column (GE Healthcare) for buffer exchange into fresh 1X HKM buffer. The sample was used as-is or purified further using HPLC. For HPLC we used a C18 column (Agilent) with a loading buffer of HPLC grade H_2O with 0.1 % trifluoroacetic acid (TFA) and a mobile phase of acetonitrile with 0.08 % TFA. The sample was collected from the column using UV-Vis at 495 nm and fractions were lyophilized and stored at -80 ^{o}C. Matrix assisted laser desorption ionization (MALDI), a soft ionization technique used to detect molecular weights, was performed on the samples at UC Berkeley's Mass Spectroscopy Facility.

Briefly the sample was diluted to 20 μM in 1:1 Acetonitrile:H_2O with 0.1% TFA. 2,5-dihydroxybenzoic acid (DHB) was used in the same solvent combination with the sample. Scans were taken up to 60,000 kDa.

The 5Fam-SAH conjugation reaction mixture or FITC-SH was utilized in tether pulling experiments similar to what is described in Chapter II. The only modification made to the experimental setup was the incubation time of the PEG-SAH or the FITC-SH was increased to 30 minutes; all other procedures and analysis were followed as described.

RESULTS AND DISCUSSION

The FITC-SH peptide in itself appears capable of lowering membrane rigidity. The peptide requires 5 % DMSO added to the buffer for solubility; the DMSO alone lowers κ_0 by ~40 %. Relative to the rigidity with DMSO and without the peptide, κ_0 is reduced by a further factor of 0.61 ± 0.15 at a peptide concentration of 0.2 μM in 0.05X HKM buffer (Figure 21) and induces membrane disintegration at concentrations $>\approx 5$ μM. For comparison, full length Sar1p lowers κ_0 by ~0.6 times at a concentration of ~5 μM (Figure 7A). We caution against drawing conclusions regarding the magnitude of the membrane softening of the peptide compared to the full-length protein, as their membrane-binding affinities may be dissimilar.

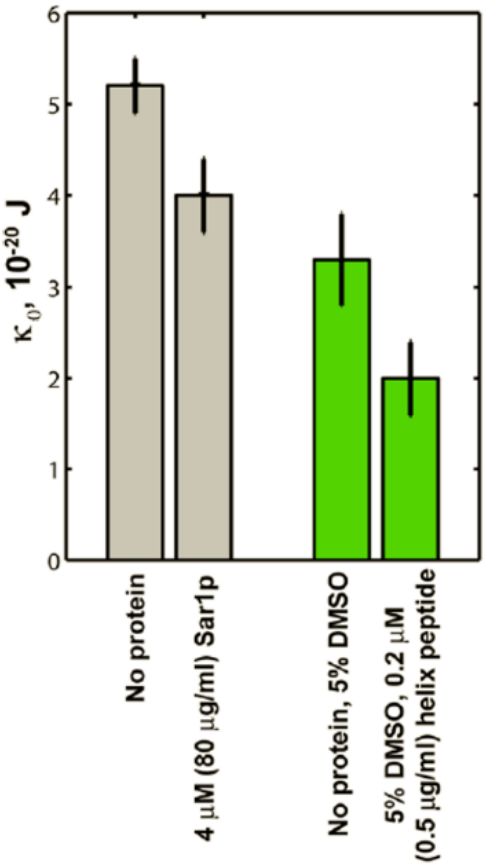

Figure 20. κ_0 for the full length Sar1p (as in Figure 7A) and a peptide corresponding to the 23 amino acid Sar1p terminal helix domain, in 0.05X HKM buffer. 5 % DMSO is required for peptide solubility, and in itself lower bilayer rigidity.

Having an understanding of the peptide's capabilities, we attempted to create an 8-arm-helical peptide using the reactive sites on the branched PEG molecule (Figure 22). The PEG molecule is ideal, as the hope is that after the reaction, PEG-5Fam-SAH would not need detergents or organics to stay soluble. Furthermore, PEG is relatively inert except for the hydrazine moieties necessary for the interaction with the peptide. We have attempted to interact our 5Fam-SAH with the 8-arm PEG hydrazine as described in our Methods and Materials section earlier in the chapter. Unfortunately, to this point we have been unsuccessful in creating a PEG-peptide species with difficulties with the conjugation reaction. Upon HPLC purification, the peptide is recovered, however results

from the mass spectral analysis by MALDI revealed no peaks associated with PEG-5Fam-SAH of any kind expected to be in the range of ~23-50 kDa (Appendix D).

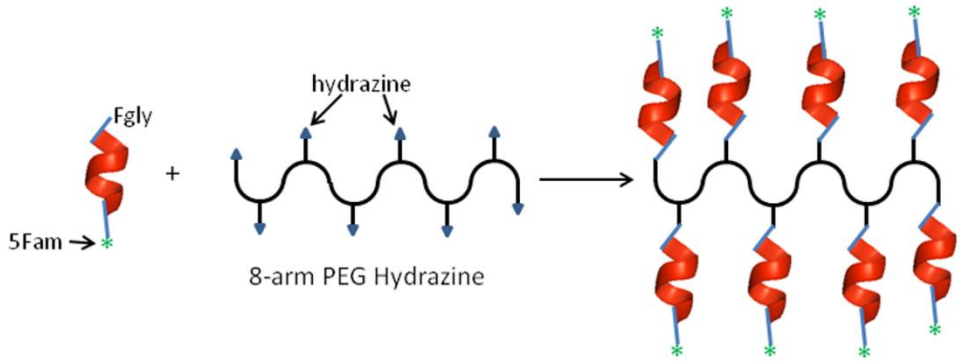

Figure 21. Schematic representation of bioconjugation between Fam5-SAH to 8-arm PEG hydrazine molecule.

This could be a two-fold problem: the reaction is not occurring due to the small amount of detergent and DMF in the solution or a degradation of the oxime bond between the PEG and peptide is occurring leaving little to no conjugated species present. In discussions with Dr. David Rabuka it is not believed to be the small amount of detergent or DMF in the solution causing the issues we have seen. Instead, our attention will be focused primarily on the parameters of the reaction. Some of the important aspects will be the reaction temperature and run time. Colder temperatures would slow the kinetics for the breakdown of the conjugation; however, the overall reaction will also run slower so a tradeoff to consider. Furthermore, we may need to adjust the pH to create a more acidic environment for the reaction mechanism to occur. The pH in most of the aldehyde tagging mechanism literature occurs at pH = 4. This may allow for an easier conjugation, though again we must consider the integrity of the peptide at lower pH. We will continue to pursue this ability to scaffold peptides together and create a system

where the possibility of reducing the membrane rigidity in a simple synthetic model is possible.

FUTURE PERSPECTIVE

As we continue working towards a complete understanding of membrane rigidity and the effects proteins have on the membrane, we are always looking to the horizon for new opportunities to explore these topics. I will provide direction towards future work to continue the research on the aforementioned topics.

Attractive membrane reducing agents we could begin to look at are specific venoms and toxins known to break down cellular membranes. These could be ideal in the production of synthetic scaffolds for membrane vesiculation as only small amounts of these proteins or peptides are necessary for membrane disruption to occur. A potential candidate for this type of work would be honeybee (*Apis mellifera*) venom. A peptide comprising 52 % of the venom is a small amphipathic alpha helix known as melittin, a known cellular lytic factor.[90,91] Additionally a number of bacterial species produce entertoxins known to alter the cellular membranes of intestinal walls. These types of toxins alter the permeability of cells and could reduce the tension and/or rigidity of the membrane. We have explored cholera toxin subunit B in the past and can continue to probe further enterotoxins for capabilities of reducing the membrane rigidity. Furthermore, we can apply our tether pulling and vesicle fluctuation assays to determine how these proteins are capable of reducing rigidity and possible candidates for peptide/protein scaffolding.

In certain diseases, understanding the effects associated proteins have on membrane physical characteristics would be of interest. Amyloid beta (Aβ) is a particular

protein, able to make plaques which degrade neuronal cells by interactions with the cell's membrane.[92,93] Aβ plaque, buildup creating radical oxygen agents to damage the neuronal cell's leading to disease such as Alzheimer's. This protein could be of particular interest as the ability to understand how rigidity and the mechanical interaction of the protein with the cell membrane is yet to be explored to my knowledge. Additionally if we have the ability to control plaque formation, it would also provide further detail to how the degradation mechanism is taking place in the context of the cellular membrane mechanics.[92-95] Beyond our *in vitro* studies, we could expand our work into directly measuring rigidity on neuronal cell cultures and how the Aβ affects the cells directly. Again, by modifying our tether pulling techniques we could create cell cultures of neuronal cells and then introduce Aβ proteins to them to investigate the affect the protein has on the cells themselves. This could provide new avenues of using our tether pulling techniques on *ex vivo* samples to provide a more comprehensive affect associated proteins have on membrane mechanics.

As I have discussed primarily proteins and peptides that associate with the membrane it would also be a unique ability to look into how integral proteins affect the membrane rigidity. We could perform studies on reconstituted membrane vesicle with incorporated proteins and observe how this changes the dynamics of rigidity. Studies on integral membrane ability have been performed[40,46] and would be helpful for elucidating certain mechanisms to vesicle trafficking. In discussions with members of Professor Elizabeth Miller's Lab (Columbia University), who are investigating the size dependence of trafficking cargo by the ER due to interactions with integral membrane proteins of the ER, it would be exciting to see what affect these integral proteins have on membrane

rigidity. By collaborating on subjects to obtain both the genetic and mechanical evidence for cargo selection and size we could provide a significant contribution to membrane trafficking and the interesting aspects leading to the membrane dynamics in cells.

CHAPTER V

CONCLUSIONS

In this dissertation, I show that (i) Sar1p monotonically reduces membrane rigidity *in vitro* to a point where the membrane itself begins to disintegrate, providing the first known example of membrane softening by a trafficking protein. (ii) Sar1A and Sar1B reduce the rigidity of the membrane to a lesser extent than Sar1p, but at higher concentrations, the rigidity increases likely due to weak protein-protein interactions creating a network on the surface of the membrane overcoming membrane reductions by the proteins. (iii) Tether pulling and vesicle fluctuation analysis each provide robust measures of membrane rigidity. (iv) The amphipathic helix of Sar1p is capable of lowering membrane rigidity by itself. I will discuss these conclusions as well as elaborate on their implications to vesicle trafficking as a whole.

We have measured the rigidity of membranes bound by the human and yeast COPII protein, Sar1. We have shown Sar1p monotonically reduces the rigidity of *in vitro* membranes to a point where disintegration of the membrane occurs. This decrease in the rigidity is due almost entirely to the ability of the protein to reduce the rigidity of the membrane and not couple to specific curvature. We speculate that this may be a common tactic among proteins with membrane-inserting motifs, such as myristoylated Arf[96,97] and proteins with N-BAR domains, the latter of which feature an amphipathic helix together with a curved, rigid form.[7,98] The widespread occurrence of N-BAR proteins at various curved intracellular surfaces, not only those whose radius conforms to the rigid BAR

crescent[98], is puzzling in the context of scaffolding, yet is sensible when viewed as related to local membrane softening. Like Sar1p, Sar1A and B paralogs are capable of lowering the membrane bending modulus, however, unlike Sar1p, the human Sar1s show increased membrane rigidity at high concentrations, concurrent with a reduction in mobility, with the concentration dependence of both of these behaviors implying the existence of protein-protein interactions. Our quantification of greater rigidity from membrane-bound Sar1A than from Sar1B may help explain phenomenological observations of different transport-related disorders[28], and different trafficking vesicle morphologies[27] induced by these two proteins. In each of these cases, Sar1B is associated with larger structures, consistent, all other things being equal, with a lower rigidity induced by this protein compared to Sar1A. More generally, the rigidity values we have measured, as well as the parameters output by a simple model of dimer-induced physical changes, should form key ingredients of potential mechanochemical models of vesicle trafficking, since rigidity determines the energetic requirements of curvature generation.[2,3,11] Such models are beginning to exist for other vesicular systems[20], and we hope to encourage their formulation for the COPII transport machinery.

Cellular membranes are non-equilibrium systems, however, and several recent studies have shown that active membrane proteins that harness energy fluxes from nucleotide hydrolysis cycles, incident light and other sources to generate molecular motion can change membrane tension and rigidity.[99-102] This raises the intriguing possibility of non-equilibrium effects beyond those explored here, especially when mediated by the full COPII complex, which employs proteins that regulate Sar1's nucleotide exchange and GTP hydrolysis rates.[13, 19, 103]

We demonstrate that SPIM-based measurements of vesicle fluctuations can be used to quantify membrane rigidity. In our studies, we provide the first demonstration of indistinguishable membrane rigidity values from tether-based and fluctuation-based assays, representing the robustness of these measurement techniques. We confirm that the trafficking protein Sar1p lowers lipid membrane rigidity and show that vesicles incubated with Sar1p exhibit the fluctuation spectra of homogeneous vesicles. In contrast, vesicles incubated with Sar1A are not well fit by a model of a homogenous membrane. This represents a limitation to the use of the theory in analyzing such systems and would need further expansion to incorporate these types of systems. In our improvement of the overall vesicle fluctuation techniques, it would be advantageous to incorporate measurements of microrheology to explore membrane viscosity of such systems. As these are already starting to occur in the laboratory, it will be fruitful to continue a dual approach to understanding the overall properties of membranes and protein-membrane systems.

Membrane softening is a known mode of action for several small peptides[11,40,104-106] and has been ascribed both to coupling to local curvature (i.e. nonzero Λ), and to direct modulation of κ by membrane thinning or increased lipid disorder. It will be interesting to further examine Sar1p's N-terminal helix alone and compare its membrane interactions with the behaviors of other, similarly sized peptides. Physically meaningful comparisons between different macromolecules, however, will require quantification of the two-dimensional concentrations of the proteins-in general, a challenging task.[107] With fluorophore conjugations, the possibility to determine these may be manageable in the future.

Beyond working with the COPII complex of proteins, we could potentially move into other trafficking schemes to understand if the mechanics work in a similar light. Some Arf and COPI proteins would be especially useful to investigate with similar structures for the ability to control the lipid membranes. Even on a more basic idea of looking at relevant changes to the lipid compositions and understanding how these changes alter the membrane rigidity would be useful as others have looked at how changes in solutions and ion concentration can alter the membrane rigidity.[108]

The potential for looking at tether pulling technique in it of itself would be of particular interest as we are watching retractions, but understanding if the same force for pulling is also occurring is of particular interest as it can reveal whether membranes are at thermal equilibrium or are governed by non-equilibrium dynamics. These types of questions and investigations will help to solidify our understanding of the techniques we are using as well as the ideas revolving around trafficking.

APPENDIX A

SUPPORTING DERIVATIONS AND METHODS FOR CHAPTER II

General principles of membrane mechanics as well as the limitations of simple continuum models described previously.[2,3,10,51-52,109] Aspects of tether mechanics are discussed in Refs. [35-37,50]. The bending energy per unit area of a membrane, ε, is a function of geometric and material parameters[11] :

$$\varepsilon = \left[\frac{\kappa}{2}(R_1^{-1} + R_2^{-1} - c_0)^2\right] + \kappa_G R_1^{-1} R_2^{-1}, \qquad \text{(Eq.S1)}$$

where R_1 and R_2 are the principle radii of curvature, c_0 is the spontaneous curvature (which gives the curvature at which the bracketed term is minimal), κ is the bending modulus (i.e. rigidity), and κ_G is the Gaussian curvature modulus.

Membrane inclusions, such as bound or inserted proteins, can change the membrane rigidity directly by altering κ (e.g. by thinning the membrane or altering lipid packing)[9,53-54], or indirectly by coupling to the local curvature and reducing the effective rigidity with respect to deformations.[10] The interaction between the inclusions and the membrane can be accounted for by additional energetic terms:

$$\varepsilon_{int} = -\Lambda\phi c + \frac{b}{2}|\nabla\phi|^2 + g(\phi), \qquad \text{(Eq.S2)}$$

where ϕ is the density of inclusions, Λ is a coupling constant, and c is the total curvature as described in Chapter II. The latter two terms describe the interactions of the intercalated particles with themselves. In general, $g(\phi)$ is not known; particular forms of

$g(\phi)$ are considered.[10,40] As described below, κ can be determined in tether-based experiments independent of the form of $g(\phi)$.

Membrane Tethers

We consider a cylindrical membrane tether of radius *R* and length L; i.e. $R_1 = R$ and $R_2 = \infty$. The total mechanical energy *E* is the sum of several terms: (i) the bending energy integrated over the cylinder area; (ii) ε_{int} integrated over the cylinder area; (iii) the elastic energy given by the product of the membrane tension, σ, and the cylinder area; and (iv) the mechanical work given by the product of the force of extension *f*, and L:

$$E = \left[\frac{\kappa}{2}(R^{-1} - 2c_0)^2 - \Lambda\phi R^{-1} + \frac{b}{2}|\nabla\phi|^2 + g(\phi) + \sigma\right] 2\pi RL - fL. \qquad \text{(Eq.S3)}$$

Neglecting non-uniformities in ϕ, this becomes:

$$E = \left[\frac{\kappa}{2}(R^{-1} - 2c_0)^2 - \Lambda\phi R^{-1} + g(\phi) + \sigma\right] 2\pi RL - fL. \qquad \text{(Eq.S4)}$$

The tether adopts the minimal energy configuration such that $\frac{\partial E}{\partial R} = 0$ and $\frac{\partial E}{\partial L} = 0$.

From the first condition:

$$\sigma + g(\phi) = \frac{\kappa}{2}(R^{-2} - 4c_0^2). \qquad \text{(Eq.S5)}$$

From the second:

$$f = \left[\frac{\kappa}{2}(R^{-1} - 2c_0)^2 - \Lambda\phi R^{-1} + g(\phi) + \sigma\right] 2\pi R. \qquad \text{(Eq.S6)}$$

Rigidity

Equations (S5) and (S6) can combine to eliminate $\sigma + g(\phi)$:

$$\frac{fR}{2\pi} = \kappa\left[1 - \left(2c_0^2 + \frac{\Lambda\phi}{\kappa}\right)R\right]. \quad \text{(Eq.S7)}$$

Several aspects of equation are worth noting. First, the coupling between the inclusions and the local curvature changes the effective spontaneous curvature, i.e. $c_0 \rightarrow c_0 + \frac{\Lambda\phi}{2\kappa}$, as in Ref. [10]. Our expression for the change in the effective spontaneous curvature differs by a factor of two from the general expression in Ref. [10] because of the one-dimensional tether curvature considered here. Second, the (unknown) self-interaction among the inclusions drops out of the derivation. Third, for a symmetric lipid bilayer membrane, as in our experiments, the bare spontaneous curvature is $c_0 = 0$. Incorporating this, and explicitly writing the possible direct inclusion-dependence of κ as $\kappa(\phi)$,

$$\frac{fR}{2\pi} = \kappa(\phi) - \Lambda\phi R. \quad \text{(Eq.S8)}$$

The functional relationship between the measureable force and radius values reveals κ and $\Lambda\phi$. Note that in the absence of coupling between the inclusions and the curvature ($\Lambda = 0$), $fR = 2\pi\kappa$, motivating our expression for the bending modulus $\kappa_0 = fR(2\pi)^{-1}$. We caution against thing of $fR(2\pi)^{-1}$ as an "effective rigidity" of the membrane from which one can predict arbitrary membrane species; general statements about effective rigidity of membranes with curvature-coupling proteins are intrinsically dependent on the form of the protein self-interaction, $g(\phi)$.[10]

Tension

Equation (S5) and (S6) can combine to eliminate κ:

$$\sigma + g(\phi) = \left(\frac{R^{-2} - 4c_0^2}{R^{-2} - 4c_0R^{-1}}\right)\left(\frac{f}{4\pi R} + \frac{\Lambda\phi}{2R}\right). \quad \text{(Eq.S9)}$$

Again using $c_0 = 0$, this simplifies to:

$$\sigma_0 = \sigma + g(\phi) = \frac{f}{4\pi R} + \frac{\Lambda\phi}{2R}. \quad \text{(Eq.S9)}$$

Where we have defined σ_0 as an effective tension that combines the (indistinguishable) bilayer tension and the self-interaction of the inclusions. If $\Lambda = 0$, $\sigma_0 = f/4\pi R$.

Methods

Approximately 5 μL of lipids dissolved in chloroform were deposited onto chambered glass coverslips. The solvent was evaporated in a vacuum desiccator for 5 min. after which the lipids were hydrated with 0.2 ml HKM buffer (20 mM Hepes-KOH, pH = 6.8, 160 mM potassium acetate, 1 mM $MgCl_2$), yielding multilayered membrane stacks. These stacks were approximately 1-2 mm in extent and the coverslip chambers were 18 mm wide, allowing ample room for the extension of tethers beyond the stack edges. For experiments with 1X (undiluted) HKM, bovine serum albumin (BSA) was adsorbed to the glass prior to lipid deposition in order to prevent van der Waals adhesion of microspheres; BSA was incubated at 1 mg/ml for several hours, followed by repeated washing. Sar1 (A, B, p) or Δ23-Sar1p, 100 μM GMPPNP (Sigma-Aldrich) and 4 mM EDTA were incubated together in an Eppendorf tube for 5m, after which they were added to the chamber containing membranes and buffer. Approximately five minutes after the addition of protein, a few microliters of a suspension of 4.8 μm diameter streptavidin-coated silica microspheres (Bangs Laboratories) were added to the chamber. The microspheres gravitationally settled and bound to the membranes.

Activation of Sar1 (binding of GMPPNP) was verified by separate experiments measuring the fluorescence emission of the tryptophan residue (Trp 84) located in the switch region of Sar1p, which serves as an indicator of protein conformation.[40,106]

Activation was found to require the presence of membranes, as in previous studies of G-proteins.[40] Data demonstrating protein activation in the presence of nucleotide, membrane, and buffer are shown in Figure S1, Appendix B. Tryptophan fluorescence emission was measured over 330-350 nm with excitation at 280 nm.

Low ionic strength (0.05X HKM) was found not to significantly inhibit Sar1-membrane binding, assessed by fluorescence microscopy of fluorophore-conjugated Sar1.

Δ23-Sar1p-GMPPNP bound to membranes containing 5 mol% DOGS-NTA-Ni at protein surface densities approximately 2x higher than wild type Sar1p-GMPPNP, as assessed by fluorescence imaging using labeled proteins. Both wild type Sar1p and Δ23-Sar1p proteins were labeled using the same labeling chemistry, noted above, and incubated with multilayered membranes, as above. Immediately after exchanging the buffer to remove unbound protein, fluorescence images of the bound protein and of fluorescent lipid probes were taken. The background-subtracted protein fluorescence intensities were normalized by the lipid fluorescence intensities to account for any changes in illumination intensity and compared to determine relative protein densities.

Lipid Bilayer Rigidity

We directly measured the bending modulus of the lipid bilayer without protein, κ_{lipid}. Alternatively, as a consistency check, we can treat κ_{lipid} as a fit parameter, using the model-fit form of the rigidity in the presence of protein to infer the rigidity as [Sar1] $\rightarrow$ 0. Doing this, we find that the fit-derived κ_{lipid} is equal within uncertainties to the value directly determined at [Sar1] = 0. These are $\kappa_{lipid} = 3.7 \pm 0.3 \times 10^{-20}$ J and $\kappa_{lipid} = 4.4 \pm 0.6 \times 10^{-20}$ J for the fit-derived and directly measured values, respectively, for data

associated with Sar1p measurements, and $\kappa_{lipid} = 6.3 \pm 0.9 \times 10^{-20}$ J and $\kappa_{lipid} = 6.6 \pm 0.4 \times 10^{-20}$ J for data associated with Sar1A and Sar1B measurements. The lipid-only rigidities are consistently different for the older measurements, taken concurrent with the Sar1p data[24], and the newer measurements taken concurrent with Sar1A and Sar1B data, independent of any experimental parameters of which we are aware, probably indicating different impurities in the commercially obtained source lipids. New experiments with Sar1p show the same lowering of rigidity observed earlier, scaled by the appropriate bare lipid rigidity.

APPENDIX B

SUPPORTING VIDEO CAPTION AND FIGURES FOR CHAPTER II

Video S1. A video of spontaneous membrane disintegration following the addition of Sar1p-GMPPNP at 17.85 μM. Width: 43 microns. Duration: 14.5 seconds. The images are of Texas Red DHPE fluorescence.

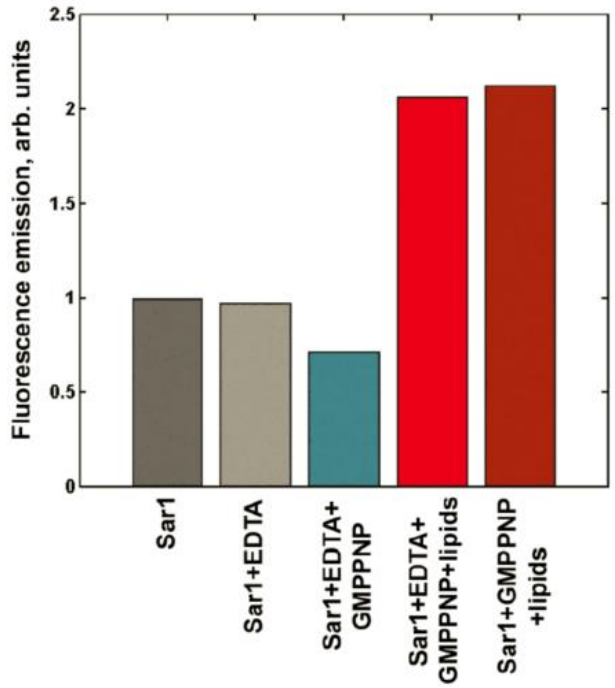

Figure S1. Tryptophan fluorescence emission and Sar1p activation. As described in Appendix A, the fluorescence of the tryptophan residue in the G-protein switch region of Sar1p and similar proteins serves as an indicator of conformation; fluorescence emission is increased in the GTP-bound state. In the absence of lipids, addition of nucleotide (bar 3) does not lead to enhanced fluorescence, but rather a drop due to UV absorption by the nucleotide. With the addition of membranes (multilamellar suspensions as in the tether assays) fluorescence is strongly enhanced, indicating nucleotide uptake (bar 4). The Sar1p concentration is 1.80 μM; the buffer and the concentrations of all other reagents are the same as in the tether pulling assays. The absence of EDTA, which chelates Mg^{2+} present in the buffer, does not significantly alter Sar1p activation (bar 5). Mg^{2+} inhibits nucleotide release and hence slows nucleotide exchange rates; in our experiments, Sar1p is not pre-loaded with nucleotide, likely explaining the lack of significance of EDTA.

APPENDIX C

SUPPORTING TABLE, VIDEO CAPTIONS AND FIGURES FOR CHAPTER III

Table S1: List of key components for Selective Plane Illumination Microscopy

Description	**Manufacturer**	**Part No.**
Laser: 594 nm	LaserMate Group, Inc.	GML593-20FLA
Scan Lens	Sill Optics	S4LFT0061/065
Excitation Objective: 5x 0.14 NA	Mitutoyo America Corp.	378-802-2
Mirror Galvonometer	Cambridge Technology	6210H
Detection Objective: 40x 1.0 NA	Carl Zeiss, Inc.	441452-9900-000
Stage: x,y,z Translation	Applied Scientific Instrumentation	LS-50 (x3)
Filter Wheel	Applied Scientific Instrumentation	FW-1000
Camera: 5.5 Mpx sCMOS	Cooke Corporation	pco.Edge

Video S2. Recording of vesicle fluctuations of a Major Mix vesicle without protein, using light sheet fluorescence microscopy. Frames per second = 60. Scale bar = 10 μm.

Video S3. Recording of vesicle fluctuations of a Major Mix vesicle incubated with 3.73 μM Sar1p using light sheet fluorescence microscopy. Frames per second = 59. Scale bar = 10 μm.

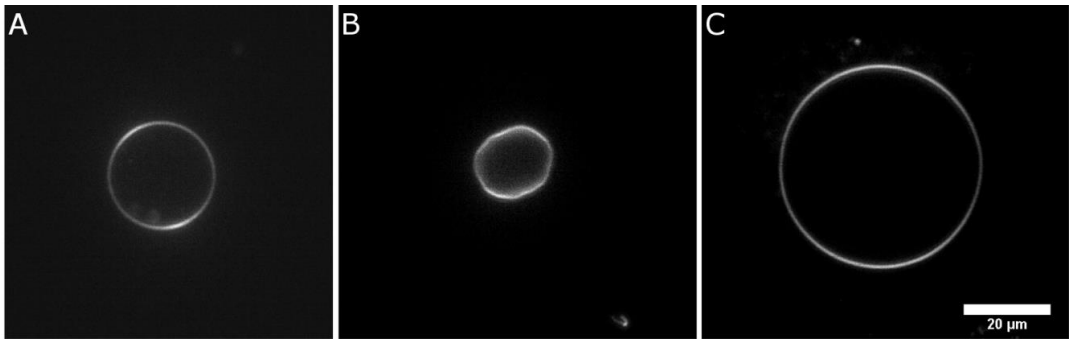

Figure S2. Giant vesicle SPIM images. (A) Major Mix vesicle (B) Vesicle incubated with 3.7 μM Sar1p + GMPPNP. (C) Vesicle incubated with 3.7 μM Sar1A + GMPPNP. Scale bar = 20 μm.

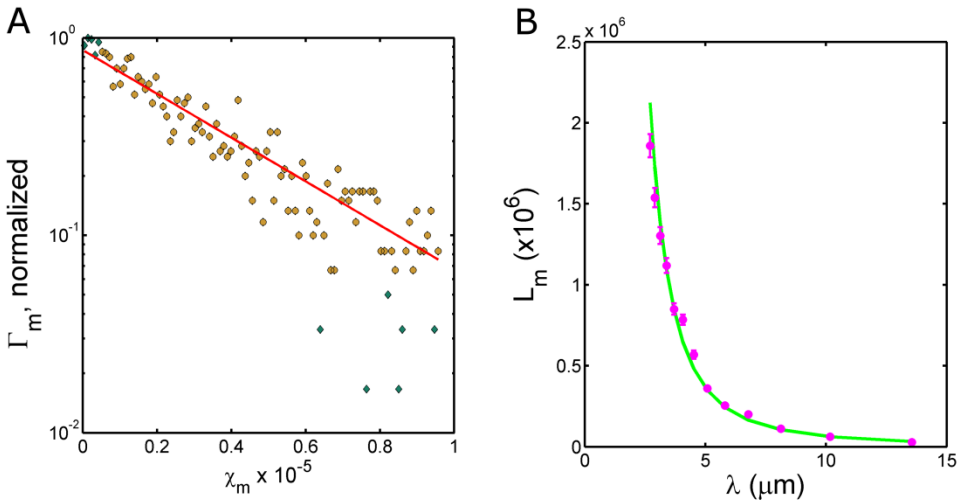

Figure S3. Fluctuation analysis of a POPC vesicle. (A) Histogram of autocorrelation amplitudes χ_m for mode m = 5 (λ = 8.13 μm) from 2000 images. The solid line is an exponential fit to the points shown in orange; the uncertainty in the fitted slope is 4 %. (D) L_m values (circles) as a function of mode wavelength ($\lambda = 2\pi R/m$) and the best-fit theoretical curve (blue line), which gives a bending modulus κ = 8.7 ± 1.1 x 10^{-20} J and tension σ = 4.6 x 10^{-8} N/m for this vesicle.

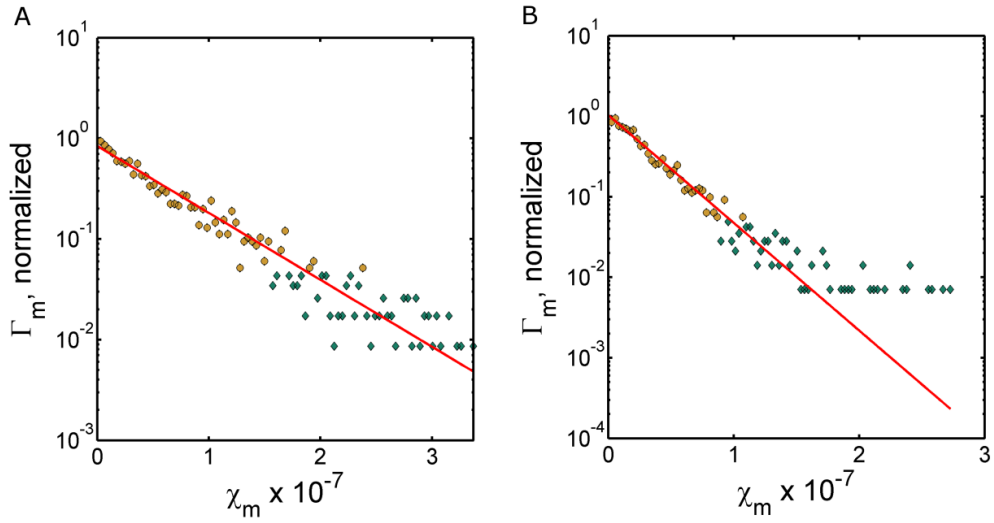

Figure S4. Histogram of autocorrelation amplitudes χ_m for mode m = 4 (λ = 30.7 μm) and m = 9 (λ = 13.6 μm) from 2000 images for a vesicle incubated with 36 μM Sar1A. The solid line is an exponential fit to the points shown in orange.

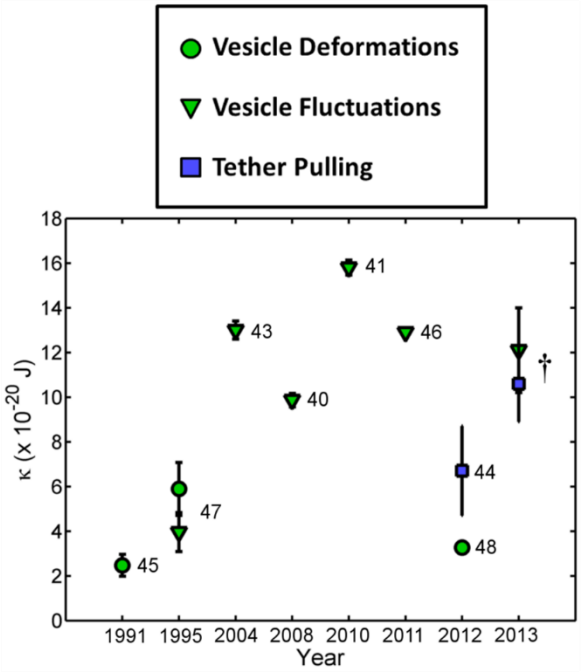

Figure S5. Bending modulus for POPC membrane assays in the literature. Values for each reference cited (green circles) vesicle deformation assays, (green triangles) thermal fluctuations of vesicles, (Purple squares) tether pulling assays. † represents data discussed in Chapter III.

APPENDIX D

SUPPORTING FIGURE FOR CHAPTER IV

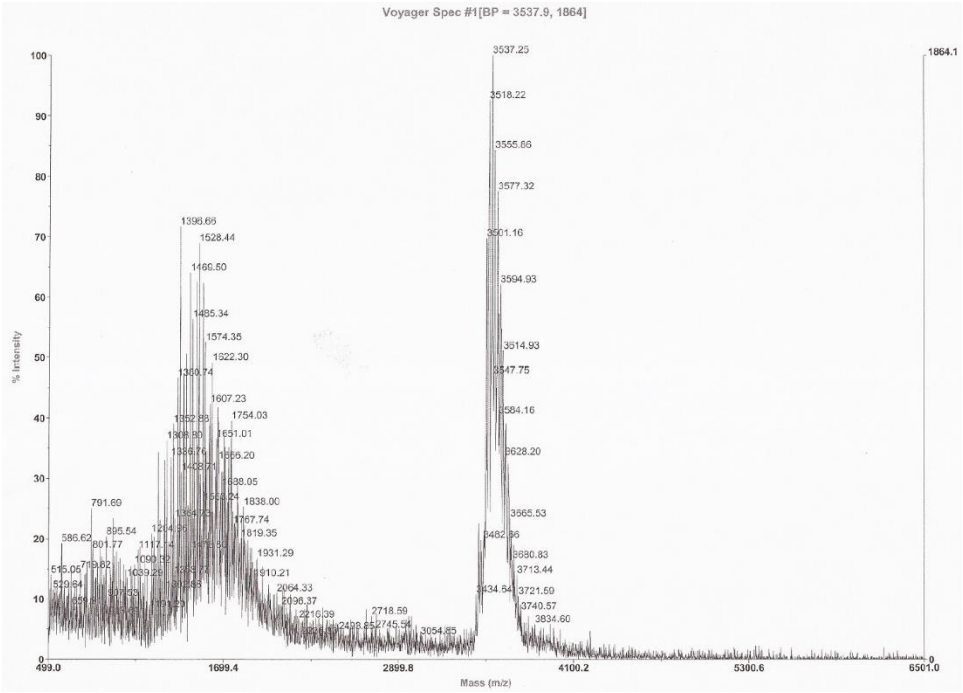

Figure S5. MALDI spectra of sample run on PEG-5Fam-SAH sample. Peak at 3537 m/z represents the peptide moiety. The scan is truncated from the original range of 60000 m/z, but beyond this range, no detectable peaks are visible above background.

REFERENCES CITED

1. Liu, Y.; Krantz, D. E.; Waites, C.; Edwards, R. H., Membrane trafficking of neurotransmitter transporters in the regulation of synaptic transmission. *Trends in Cell Biology* **1999,** *9* (9), 356-363.

2. Zimmerberg, J.; Kozlov, M. M., How proteins produce cellular membrane curvature. *Nature Reviews Molecular Cell Biology* **2006,** *7* (1), 9-19.

3. Parthasarathy, R.; Groves, J. T., Curvature and spatial organization in biological membranes. *Soft Matter* **2007,** *3* (1), 24-33.

4. Baumgart, T.; Capraro, B. R.; Zhu, C.; Das, S. L., Thermodynamics and mechanics of membrane curvature generation and sensing by proteins and lipids. *Annual Review of Physical Chemistry* **2011,** *62* (1), 483-506.

5. Frost, A.; Perera, R.; Roux, A.; Spasov, K.; Destaing, O.; Egelman, E. H.; De Camilli, P.; Unger, V. M., Structural Basis of Membrane Invagination by F-BAR Domains. *Cell* **2008,** *132* (5), 807-817.

6. Pearse, B. M. F.; Smith, C. J.; Owen, D. J., Clathrin coat construction in endocytosis. *Current Opinion in Structural Biology* **2000,** *10* (2), 220-228.

7. Peter, B. J.; Kent, H. M.; Mills, I. G.; Vallis, Y.; Butler, P. J. G.; Evans, P. R.; McMahon, H. T., BAR domains as sensors of membrane curvature: the amphiphysin BAR structure. *Science* **2004,** *303* (5657), 495-499.

8. Stagg, S. M.; Gurkan, C.; Fowler, D. M.; LaPointe, P.; Foss, T. R.; Potter, C. S.; Carragher, B.; Balch, W. E., Structure of the Sec13/31 COPII coat cage. *Nature* **2006,** *439* (7073), 234-238.

9. Huang, H. W., Molecular mechanism of antimicrobial peptides: the origin of cooperativity. *Biochimica et Biophysica Acta (BBA) - Biomembranes* **2006,** *1758* (9), 1292-1302.

10. Leibler, S., Curvature instability in membranes. *Journal de Physique France* **1986,** *47* (3), 507-516.

11. McMahon, H. T.; Gallop, J. L., Membrane curvature and mechanisms of dynamic cell membrane remodelling. *Nature* **2005,** *438* (7068), 590-596.

12. Phillips, R.; Tristan, U.; Paul, W.; Pierre, S., Emerging roles for lipids in shaping membrane-protein function. *Nature* **2009,** *459* (7245), 379-385.

13. Lee, M. C.; Miller, E. A.; Goldberg, J.; Orci, L.; Schekman, R., Bi-directional protein transport between the ER and Golgi. *Annual Review of Cell and Development Biology* **2004,** *20*, 87-123.

14. Matsuoka, K.; Orci, L.; Amherdt, M.; Bednarek, S. Y.; Hamamoto, S.; Schekman, R.; Yeung, T., COPII-coated vesicle formation reconstituted with purified coat proteins and chemically defined liposomes. *Cell* **1998,** *93* (2), 263-275.

15. Lee, M. C. S.; Orci, L.; Hamamoto, S.; Futai, E.; Ravazzola, M.; Schekman, R., Sar1p N-terminal helix initiates membrane curvature and completes the fission of a COPII vesicle. *Cell* **2005,** *122* (4), 605-617.

16. Bielli, A.; Haney, C. J.; Gabreski, G.; Watkins, S. C.; Bannykh, S. I.; Aridor, M., Regulation of Sar1 NH2 terminus by GTP binding and hydrolysis promotes membrane deformation to control COPII vesicle fission. *The Journal of Cell Biology* **2005,** *171* (6), 919-924.

17. Yoshihisa, T.; Barlowe, C.; Schekman, R., Requirement for a GTPase-activating protein in vesicle budding from the endoplasmic reticulum. *Science* **1993,** *259* (5100), 1466-1468.

18. Miller, E.; Antonny, B.; Hamamoto, S.; Schekman, R., Cargo selection into COPII vesicles is driven by the Sec24p subunit. *The European Molecular Biology Organization Journal* **2002,** *21* (22), 6105-6113.

19. Lee, M. C. S.; Miller, E. A., Molecular mechanisms of COPII vesicle formation. *Seminars in Cell and Developmental Biology* **2007,** *18* (4), 424-434.

20. Antonny, B.; Madden, D.; Hamamoto, S.; Orci, L.; Schekman, R., Dynamics of the COPII coat with GTP and stable analogues. *Nature Cell Biology* **2001,** *3* (6), 531-537.

21. Barlowe, C.; Schekman, R., SEC12 encodes a guanine-nucleotide-exchange factor essential for transport vesicle budding from the ER. *Nature* **1993,** *365* (6444), 347-349.

22. Rao, Y.; Bian, C.; Yuan, C.; Li, Y.; Chen, L.; Ye, X.; Huang, Z.; Huang, M., An open conformation of switch I revealed by Sar1-GDP crystal structure at low Mg^{2+}. *Biochemical and Biophysical Research Communications* **2006,** *348* (3), 908-915.

23. Bi, X.; Corpina, R. A.; Goldberg, J., Structure of the Sec23/24-Sar1 pre-budding complex of the COPII vesicle coat. *Nature* **2002,** *419* (6904), 271-277.

24. Huang, M.; Weissman, J. T.; Béraud-Dufour, S.; Luan, P.; Wang, C.; Chen, W.; Aridor, M.; Wilson, I. A.; Balch, W. E., Crystal structure of Sar1-GDP at 1.7 Å resolution and the role of the NH2 terminus in ER export. *The Journal of Cell Biology* **2001,** *155* (6), 937-948.

25. Wang, J.; Dimov, S.; Tempel, W.; Yaniw, D.; Arrowsmith, C.; Edwards, A.; Sundstrom, M.; Weigelt, J.; Bochkarev, A.; Park, H., PDB ID: 2GAO.

26. Zanetti, G.; Pahuja, K. B.; Studer, S.; Shim, S.; Schekman, R., COPII and the regulation of protein sorting in mammals. *Nature Cell Biology* **2011,** *14* (1), 20-28.

27. Fromme, J. C.; Orci, L.; Schekman, R., Coordination of COPII vesicle trafficking by Sec23. *Trends in Cell Biology* **2008,** *18* (7), 330-336.

28. Jones, B.; Jones, E. L.; Bonney, S. A.; Patel, H. N.; Mensenkamp, A. R.; Eichenbaum-Voline, S.; Rudling, M.; Myrdal, U.; Annesi, G.; Naik, S.; Meadows, N.; Quattrone, A.; Islam, S. A.; Naoumova, R. P.; Angelin, B.; Infante, R.; Levy, E.; Roy, C. C.; Freemont, P. S.; Scott, J.; Shoulders, C. C., Mutations in a Sar1 GTPase of COPII vesicles are associated with lipid absorption disorders. *Nature Genetics* **2003,** *34* (1), 29-31.

29. Sheetz, M. P.; Singer, S., Biological membranes as bilayer couples. A molecular mechanism of drug-erythrocyte interactions. *Proceedings of the National Academy of Sciences* **1974,** *71* (11), 4457-4461.

30. Sheetz, M. P.; Painter, R. G.; Singer, S., Biological membranes as bilayer couples. *Journal of Cell Biology* **1976,** *70*, 193-203.

31. Neuman, K. C.; Block, S. M., Optical trapping. *Review of Scientific Instruments* **2004,** *75* (9), 2787-2809.

32. Ashkin, A.; Dziedzic, J.; Yamane, T., Optical trapping and manipulation of single cells using infrared laser beams. *Nature* **1987,** *330* (6150), 769-771.

33. Raab, E.; Prentiss, M.; Cable, A.; Chu, S.; Pritchard, D. E., Trapping of neutral sodium atoms with radiation pressure. *Physical Review Letters* **1987,** *59* (23), 2631.

34. Borghi, N.; Brochard-Wyart, F., Tether extrusion from red blood cells: integral proteins unbinding from cytoskeleton. *Biophysical Journal* **2007,** *93* (4), 1369-1379.

35. Dai, J.; Sheetz, M. P., Mechanical properties of neuronal growth cone membranes studied by tether formation with laser optical tweezers. *Biophysical Journal* **1995,** *68* (3), 988-996.

36. Derényi, I.; Jülicher, F.; Prost, J., Formation and interaction of membrane tubes. *Physical Review Letters* **2002,** *88* (23), 238101.

37. Powers, T. R.; Huber, G.; Goldstein, R. E., Fluid-membrane tethers: minimal surfaces and elastic boundary layers. *Physical Review E* **2002,** *65* (4), 041901.

38. Raucher, D.; Sheetz, M. P., Characteristics of a membrane reservoir buffering membrane tension. *Biophysical Journal* **1999,** *77* (4), 1992-2002.

39. Sorre, B.; Callan-Jones, A.; Manneville, J.-B.; Nassoy, P.; Joanny, J.-F.; Prost, J.; Goud, B.; Bassereau, P., Curvature-driven lipid sorting needs proximity to a demixing point and is aided by proteins. *Proceedings of the National Academy of Sciences* **2009,** *106* (14), 5622-5626.

40. Bouvrais, H.; Méléard, P.; Pott, T.; Jensen, K. J.; Brask, J.; Ipsen, J. H., Softening of POPC membranes by magainin. *Biophysical Chemistry* **2008,** *137* (1), 7-12.

41. Bouvrais, H.; Pott, T.; Bagatolli, L. A.; Ipsen, J. H.; Méléard, P., Impact of membrane-anchored fluorescent probes on the mechanical properties of lipid bilayers. *Microscopy Imaging of Membrane Domains* **2010,** *1798* (7), 1333-1337.

42. Faucon, J. F.; Mitov, M. D.; Méléard, P.; Bivas, I.; Bothorel, P., Bending elasticity and thermal fluctuations of lipid membranes. Theoretical and experimental requirements. *Journal de Physique France* **1989,** *50* (17), 2389-2414.

43. Henriksen, J.; Rowat, A.; Ipsen, J., Vesicle fluctuation analysis of the effects of sterols on membrane bending rigidity. *European Biophysical Journal* **2004,** *33* (8), 732-741.

44. Kocun, M.; Janshoff, A., Pulling tethers from pore-spanning bilayers: towards simultaneous determination of local bending modulus and lateral tension of membranes. *Small* **2012,** *8* (6), 847-851.

45. Kummrow, M.; Helfrich, W., Deformation of giant lipid vesicles by electric fields. *Physical Review A* **1991,** *44* (12), 8356-8360.

46. Méléard, P.; Pott, T.; Bouvrais, H.; Ipsen, J. H., Advantages of statistical analysis of giant vesicle flickering for bending elasticity measurements. *European Physical Journal E* **2011,** *34* (10), 1-14.

47. Niggemann, G.; Kummrow, M.; Helfrich, W., The bending rigidity of phosphatidylcholine bilayers: dependences on experimental method, sample cell sealing and Temperature. *Journal de Physique II France* **1995,** *5* (3), 413-425.

48. Solmaz, M. E.; Biswas, R.; Sankhagowit, S.; Thompson, J. R.; Mejia, C. A.; Malmstadt, N.; Povinelli, M. L., Optical stretching of giant unilamellar vesicles with an integrated dual-beam optical trap. *Biomedical Optical Express* **2012,** *3* (10), 2419-2427.

49. Carrico, I. S.; Carlson, B. L.; Bertozzi, C. R., Introducing genetically encoded aldehydes into proteins. *Nature Chemical Biology* **2007,** *3* (6), 321-322.

50. Waugh, R. E.; Hochmuth, R. M., Mechanical equilibrium of thick, hollow, liquid membrane cylinders. *Biophysical Journal* **1987,** *52* (3), 391-400.

51. Helfrich, W., Elastic properties of lipid bilayers: theory and possible experiments. *Zeitschrift für Naturforschung. Teil C: Biochemie, Biophysik, Biologie, Virologie* **1973,** *28* (11), 693.

52. Lipowsky, R.; Sackmann, E., *Structure and Dynamics of Membranes: I. From Cells to Vesicles/II. Generic and Specific Interactions*. Elsevier, NY: 1995.

53. Huang, H. W., Elasticity of lipid bilayer interacting with amphiphilic helical peptides. *Journal de Physique II* **1995,** *5* (10), 1427-1431.

54. Pan, J.; Tieleman, D. P.; Nagle, J. F.; Kučerka, N.; Tristram-Nagle, S., Alamethicin in lipid bilayers: combined use of X-ray scattering and MD simulations. *Biochimica et Biophysica Acta (BBA)-Biomembranes* **2009,** *1788* (6), 1387-1397.

55. Jähnig, F., What is the surface tension of a lipid bilayer membrane? *Biophysical Journal* **1996,** *71* (3), 1348.

56. Matsuoka, K., COPII-coated vesicle formation reconstituted with purified coat proteins and chemically defined liposomes. *Cell* **1998,** *93*, 263-275.

57. Bustamante, C.; Macosko, J. C.; Wuite, G. J., Grabbing the cat by the tail: manipulating molecules one by one. *Nature Reviews Molecular Cell Biology* **2000,** *1* (2), 130-136.

58. Moffitt, J. R.; Chemla, Y. R.; Smith, S. B.; Bustamante, C., Recent advances in optical tweezers. *Annual Review of Biochemistry* **2008,** *77*, 205-228.

59. Sainis, S. K.; Germain, V.; Dufresne, E. R., Statistics of particle trajectories at short time intervals reveal fN-scale colloidal forces. *Physical Review Letters* **2007,** *99* (1).

60. Evans, E.; Yeung, A., Hidden dynamics in rapid changes of bilayer shape. *Chemistry and Physics of Lipids* **1994,** *73* (1), 39-56.

61. Antonny, B.; Huber, I.; Paris, S.; Chabre, M.; Cassel, D., Activation of ADP-ribosylation factor 1 GTPase-activating protein by phosphatidylcholine-derived diacylglycerols. *Journal of Biological Chemistry* **1997,** *272* (49), 30848-30851.

62. Duda, R. O.; Hart, P. E., Use of the Hough transformation to detect lines and curves in pictures. *Communications of the Association of Computing Machinery* **1972,** *15* (1), 11-15.

63. Crocker, J. C.; Grier, D. G., Methods of digital video microscopy for colloidal studies. *Journal of Colloid and Interface Science* **1996,** *179* (1), 298-310.

64. Schneider, M.; Jenkins, J.; Webb, W., Thermal fluctuations of large cylindrical phospholipid vesicles. *Biophysical Journal* **1984,** *45* (5), 891-899.

65. Jo, S.; Vargyas, M.; Vasko-Szedlar, J.; Roux, B.; Im, W., PBEQ-Solver for online visualization of electrostatic potential of biomolecules. *Nucleic Acids Research* **2008,** *36* (suppl 2), W270-W275.

66. Axelrod, D.; Koppel, D. E.; Schlessinger, J.; Elson, E.; Webb, W. W., Mobility measurement by analysis of fluorescence photobleaching recovery kinetics. *Biophysical Journal* **1976,** *16* (9), 1055-1069.

67. Harland, C. W.; Rabuka, D.; Bertozzi, C. R.; Parthasarathy, R., The mycobacterium tuberculosis virulence factor trehalose dimycolate imparts desiccation resistance to model mycobacterial membranes. *Biophysical Journal* **2008,** *94* (12), 4718-4724.

68. Gygi, S. P.; Rochon, Y.; Franza, B. R.; Aebersold, R., Correlation between protein and mRNA abundance in yeast. *Molecular and Cellular Biology* **1999,** *19* (3), 1720-1730.

69. Harland, C. W.; Botyanszki, Z.; Rabuka, D.; Bertozzi, C. R.; Parthasarathy, R., Synthetic trehalose glycolipids confer desiccation resistance to supported lipid monolayers. *Langmuir* **2009,** *25* (9), 5193-5198.

70. Shimada, A.; Niwa, H.; Tsujita, K.; Suetsugu, S.; Nitta, K.; Hanawa-Suetsugu, K.; Akasaka, R.; Nishino, Y.; Toyama, M.; Chen, L.; Liu, Z.-J.; Wang, B.-C.; Yamamoto, M.; Terada, T.; Miyazawa, A.; Tanaka, A.; Sugano, S.; Shirouzu, M.; Nagayama, K.; Takenawa, T.; Yokoyama, S., Curved EFC/F-BAR-domain dimers are joined end to end into a filament for membrane invagination in endocytosis. *Cell* **2007,** *129* (4), 761-772.

71. Ramamurthi, K. S.; Lecuyer, S.; Stone, H. A.; Losick, R., Geometric cue for protein localization in a bacterium. *Science* **2009,** *323* (5919), 1354-1357.

72. Bigay, J.; Casella, J.-F.; Drin, G.; Mesmin, B.; Antonny, B., ArfGAP1 responds to membrane curvature through the folding of a lipid packing sensor motif. *The European Molecular Biology Organization Journal* **2005,** *24* (13), 2244-2253.

73. Wang, Y.-H.; Collins, A.; Guo, L.; Smith-Dupont, K. B.; Gai, F.; Svitkina, T.; Janmey, P. A., Divalent cation-induced cluster formation by polyphosphoinositides in model membranes. *Journal of the American Chemical Society* **2012,** *134* (7), 3387-3395.

74. Rossier, O.; Cuvelier, D.; Borghi, N.; Puech, P. H.; Derényi, I.; Buguin, A.; Nassoy, P.; Brochard-Wyart, F., Giant vesicles under flows: extrusion and retraction of tubes. *Langmuir* **2003,** *19* (3), 575-584.

75. Pécréaux, J.; Döbereiner, H. G.; Prost, J.; Joanny, J. F.; Bassereau, P., Refined contour analysis of giant unilamellar vesicles. *European Physical Journal E* **2004,** *13* (3), 277-290.

76. Méléard, P.; Gerbeaud, C.; Pott, T.; Fernandez-Puente, L.; Bivas, I.; Mitov, M. D.; Dufourcq, J.; Bothorel, P., Bending elasticities of model membranes: influences of temperature and sterol content. *Biophysical Journal* **1997,** *72* (6), 2616-2629.

77. Gracia, R. S.; Bezlyepkina, N.; Knorr, R. L.; Lipowsky, R.; Dimova, R., Effect of cholesterol on the rigidity of saturated and unsaturated membranes: fluctuation and electrodeformation analysis of giant vesicles. *Soft Matter* **2010,** *6* (7), 1472-1482.

78. Huisken, J.; Stainier, D. Y. R., Selective plane illumination microscopy techniques in developmental biology. *Development* **2009,** *136* (12), 1963-1975.

79. Jemielita, M.; Taormina, M. J.; DeLaurier, A.; Kimmel, C. B.; Parthasarathy, R., Comparing phototoxicity during the development of a zebrafish craniofacial bone using confocal and light sheet fluorescence microscopy techniques. *Journal of Biophotonics* **2012**, 11-12.

80. Keller, P. J.; Schmidt, A. D.; Wittbrodt, J.; Stelzer, E. H. K., Reconstruction of zebrafish early embryonic development by scanned light sheet microscopy. *Science* **2008,** *322* (5904), 1065-1069.

81. Ntziachristos, V., Going deeper than microscopy: the optical imaging frontier in biology. *Nature Methods* **2010,** *7* (8), 603-614.

82. Taormina, M. J.; Jemielita, M.; Stephens, W. Z.; Burns, A. R.; Troll, J. V.; Parthasarathy, R.; Guillemin, K., Investigating bacterial-animal symbioses with light sheet microscopy. *The Biological Bulletin* **2012,** *223* (1), 7-20.

83. Barlowe, C.; d'Enfert, C.; Schekman, R., Purification and characterization of SAR1p, a small GTP-binding protein required for transport vesicle formation from the endoplasmic reticulum. *Journal of Biological Chemistry* **1993,** *268* (2), 873-879.

84. Parthasarathy, R., Rapid, accurate particle tracking by calculation of radial symmetry centers. *Nature Methods* **2012,** *9* (7), 724-726.

85. Herold, C.; Chwastek, G.; Schwille, P.; Petrov, E. P., Efficient electroformation of supergiant unilamellar vesicles containing cationic lipids on ITO-coated electrodes. *Langmuir* **2012,** *28* (13), 5518-5521.

86. Groves, J. T.; Parthasarathy, R.; Forstner, M. B., Fluorescence imaging of membrane dynamics. *Annual Review of Biomedical Engineering.* **2008,** *10* (1), 311-338.

87. Wolff, L., Chemischen institut der Universität Jena: methode zum ersatz des sauerstoffatoms der ketone und aldehyde durch wasserstoff.[Erste Abhandlung.]. *Justus Liebigs Annalen der Chemie* **1912,** *394* (1), 86-108.

88. Kishner, N., Benzoyl iodide and its relation to ether. *Journal of the Russian Chemical Society* **1911,** *43*, 582.

89. Rabuka, D.; Rush, J. S.; W deHart, G.; Wu, P.; Bertozzi, C. R., Site-specific chemical protein conjugation using genetically encoded aldehyde tags. *Nature Protocols* **2012,** *7* (6), 1052-1067.

90. Berneche, S.; Nina, M.; Roux, B., Molecular dynamics simulation of melittin in a dimyristoylphosphatidylcholine bilayer membrane. *Biophysical Journal* **1998,** *75* (4), 1603-1618.

91. Andersson, A.; Biverståhl, H.; Nordin, J.; Danielsson, J.; Lindahl, E.; Mäler, L., The membrane-induced structure of melittin is correlated with the fluidity of the lipids. *Biochimica et Biophysica Acta (BBA)-Biomembranes* **2007,** *1768* (1), 115-121.

92. Gibson Wood, W.; Eckert, G. P.; Igbavboa, U.; Müller, W. E., Amyloid beta-protein interactions with membranes and cholesterol: causes or casualties of Alzheimer's disease. *Biochimica et Biophysica Acta (BBA)-Biomembranes* **2003,** *1610* (2), 281-290.

93. Eckert, G.; Cairns, N.; Maras, A.; Gattaz, W.; Müller, W., Cholesterol modulates the membrane-disordering effects of beta-amyloid peptides in the hippocampus: specific changes in Alzheimer's disease. *Dementia and geriatric cognitive disorders* **2000,** *11* (4), 181-186.

94. Kim, J.; Hamamoto, S.; Ravazzola, M.; Orci, L.; Schekman, R., Uncoupled packaging of amyloid precursor protein and presenilin 1 into COPII vesicles. *Journal of Biological Chemistry* **2005,** *280*, 7758-7768.

95. Kim, D. H.; Frangos, J. A., Effects of Amyloid β-Peptides on the Lysis Tension of Lipid Bilayer Vesicles Containing Oxysterols. *Biophysical Journal* **2008,** *95* (2), 620-628.

96. Goldberg, J., Structural basis for activation of ARF GTPase: mechanisms of guanine nucleotide exchange and GTP–myristoyl switching. *Cell* **1998,** *95* (2), 237-248.

97. Beck, R.; Sun, Z.; Adolf, F.; Rutz, C.; Bassler, J.; Wild, K.; Sinning, I.; Hurt, E.; Brügger, B.; Béthune, J., Membrane curvature induced by Arf1-GTP is essential for vesicle formation. *Proceedings of the National Academy of Sciences* **2008,** *105* (33), 11731-11736.

98. Itoh, T.; De Camilli, P., BAR, F-BAR (EFC) and ENTH/ANTH domains in the regulation of membrane–cytosol interfaces and membrane curvature. *Biochimica et Biophysica Acta (BBA)-Molecular and Cell Biology of Lipids* **2006,** *1761* (8), 897-912.

99. Manneville, J.-B.; Bassereau, P.; Levy, D.; Prost, J., Activity of transmembrane proteins induces magnification of shape fluctuations of lipid membranes. *Physical Review Letters* **1999,** *82* (21), 4356.

100. Faris, M.; Lacoste, D.; Pécréaux, J.; Joanny, J.; Prost, J.; Bassereau, P., Membrane tension lowering induced by protein activity. *arXiv:0807.0081[cond-mat.soft]* **2008**.

101. Girard, P.; Prost, J.; Bassereau, P., Passive or active fluctuations in membranes containing proteins. *Physical Review Letters* **2005,** *94* (8), 088102.

102. Betz, T.; Lenz, M.; Joanny, J.-F.; Sykes, C., ATP-dependent mechanics of red blood cells. *Proceedings of the National Academy of Sciences* **2009,** *106* (36), 15320-15325.

103. Gürkan, C.; Stagg, S. M.; LaPointe, P.; Balch, W. E., The COPII cage: unifying principles of vesicle coat assembly. *Nature Reviews Molecular Cell Biology* **2006,** *7* (10), 727-738.

104. Häckl, W.; Seifert, U.; Sackmann, E., Effects of fully and partially solubilized amphiphiles on bilayer bending stiffness and temperature dependence of the effective tension of giant vesicles. *Journal de Physique II* **1997,** *7* (8), 1141-1157.

105. Vitkova, V.; Méléard, P.; Pott, T.; Bivas, I., Alamethicin influence on the membrane bending elasticity. *European Biophysical Journal* **2006,** *35* (3), 281-286.

106. Tristram-Nagle, S.; Nagle, J. F., HIV-1 fusion peptide decreases bending energy and promotes curved fusion intermediates. *Biophysical Journal* **2007,** *93* (6), 2048-2055.

107. Galush, W. J.; Nye, J. A.; Groves, J. T., Quantitative fluorescence microscopy using supported lipid bilayer standards. *Biophysical Journal* **2008,** *95* (5), 2512-2519.

108. Bouvrais, H.; Duelund, L.; Ipsen, J. H., Buffers affect the bending rigidity of model lipid membranes. *Langmuir* **2013,** *30* (1), 13-16.

109. Safran, S. A., *Statistical thermodynamics of surfaces, interfaces, and membranes*. Addison-Wesley Reading, MA: 1994.